Controlling plasma produced fluxes to liquid surfaces by acoustic structuring: applications to plasma driven solution electrochemistry

Scott J Doyle[1] ![ORCID]**, Tiago C Dias** ![ORCID]**, Mackenzie Meyer**[2] ![ORCID]
and Mark J Kushner[*] ![ORCID]

Department of Electrical Engineering and Computer Science, University of Michigan, Ann Arbor, MI 48109-2122, United States of America

E-mail: mjkush@umich.edu, scott.doyle@physics.org, tiagocd@umich.edu and maemeyer@umich.edu

CrossMark

Abstract

Plasmas interacting with liquid surfaces produce a complex interfacial layer where the local chemistry in the liquid is driven by fluxes from the gas phase of electrons, ions, photons, and neutral radicals. Typically, the liquid surface has at best mild curvature with the fluxes of impinging plasma species and applied electric field being nominally normal to the surface. With liquids such as water having a high dielectric constant, structuring of the liquid surface by producing a wavy surface enables local electric field enhancement due to polarization of the liquid, as well as producing regions of higher and lower advective gas flow across the surface. This structuring (or waviness) can naturally occur or can be achieved by mechanical agitation such as with acoustic transducers. Electric field enhancement at the peaks of the waves of the liquid produces local increases in sources of reactive species and incident plasma fluxes which may be advantageous for plasma driven solution electrochemistry (PDSE) applications. In this paper, results are discussed from a computational investigation of pulsed atmospheric pressure plasma jets onto structured water solutions containing $AgNO_3$ as may be used in PDSE for silver nanoparticle (NP) formation. The solution surface consists of standing wave patterns having wavelength and wave depth of hundreds of microns to 1 mm. The potential for structured liquid surfaces to facilitate spatially differentiated chemical selectivity and enhance NP synthesis in the context of PDSE is discussed.

1. Introduction

Plasma driven solution electrochemistry (PDSE) broadly refers to the delivery of plasma produced species to an electrolytic cell or an isolated electrolytic solution with the goal being material synthesis or chemical conversion. In these applications, the externally applied low-temperature plasma can serve as either the cathode or anode [1–3]. PDSE differs from other plasma-assisted electrolysis techniques, such as contact glow-discharge electrolysis [4–7], where electrodes are immersed within the electrolyte. In PDSE, a plasma impinging onto a liquid electrolyte acts as a reducing or oxidizing agent in place of, for example, a solid cathode immersed within the solution [8–10]. Plasma-assisted electrochemical processes differ from conventional electrochemical processes due primarily to the wide range of plasma produced species delivered to the solution, including electrons, ions, photons, and neutral radicals, that may affect or stimulate the material synthesis process.

When the solution acts as the anode, large fluxes of electrons can be incident onto the plasma–liquid interface. Once in the solution, electrons will typically solvate prior to reacting with other in-solution species. Excited atomic and molecular species in the gas phase produce UV and VUV photons that penetrate into the solution. With most applications of PDSE being performed at atmospheric pressure, the plasma on the surface of the solution is usually in the form of a surface ionization wave (SIW) which hugs the surface. As a result, these plasma produced photons are directed into the liquid, representing a significant source for dissociation and ionization of solution resident species [11]. Plasma produced electrons and photons typically directly interact with the top tens to hundreds of nm [12–15] of the liquid. Longer lived gas phase ions and neutral radical species also transport across the plasma–liquid interface and either rapidly react with liquid phase species in the interfacial layer or diffuse deeper into the solution. Neutral species such as OH react quickly in the liquid whereas longer lived species such as H_2O_2 will diffuse deeper into the solution.

The majority of PDSE applications employ either a pulsed atmospheric pressure plasma jet (APPJ) or a DC glow discharge, the latter which typically requires a conductive solution and counter electrode to sustain the DC current [1, 2]. Pulsed plasma jets are of particular interest as the rapidly rising voltage pulse (typically $\approx$10–100 ns rise time) produces high transient electric fields that significantly exceed those in steady state sources [1]. Pulsing such sources can produce time averaged reactive fluxes that exceed their DC counterparts.

Metal and semiconductor nanoparticles (NPs) are employed as catalysts, microelectronics components, optical components, biomedical delivery or material coating agents, and recently as additives to battery and fuel cell electrodes to enhance charge density [16, 17]. Silver NPs (Ag NP) account for $\approx$55% of nanomaterial-based consumer goods [18], due primarily to their high electrical and thermal conductivities, catalytic activity, and antibacterial properties [19]. The catalytic, optical, and electrical properties of NPs depend on their size and shape; and so it is important to control these properties. A wide range of methods have been employed to control NP growth and morphology in both conventional solutions and PDSE, including choice of the NP precursor species and molarity [20], growth medium temperature [21], plasma treatment time [22], and the addition of capping agents [23]. The addition of capping agents or stabilizing agents influences the NP size and morphology, enabling spheres, rods, cubes, prisms, or irregular shapes [19, 20, 23]. Common capping agents include ammonia, paraffin, dimethylformamide, trisodium citrate, polyethylene glycol, glycerol, sucrose, and other ligand polymer additives [18, 23].

Plasma-assisted NP production as an alternative to conventional methods has been investigated in both the gas [17, 24] and liquid phase [22, 25, 26]. In general, PDSE NP synthesis reduces or removes the need for chemical reducing agents, while potentially providing precise control of NP size and morphology [18]. However, there are several unknowns regarding the physical, chemical, and electrical effects of electron, ion, and radical transport across plasma–liquid interfaces, and the role(s) that solvated atomic and molecular reducing species such as OH⁻ and O⁻ have on NP growth.

In a prior work, SIW propagation across wavy dielectric surfaces was investigated [27]. It was found that the polarization of the dielectric (which increases the electric field in the gas phase at the surface of the dielectric) combined with geometrical electric field enhancement at the apexes of the waves results in directing electron fluxes into the apexes (or peaks of the wave). The ratio of, for example, electron to VUV fluences to the surface can be controlled by the depth and wavelength of the modulated surface. Although PDSE solutions are conductive, they respond as dielectrics if their dielectric relaxation time is longer than the pulse length of the plasma. In this regard, wavy electrolytic solutions will likely affect the propagation of SIWs across their surfaces in a similar manner as wavy dielectrics—focusing of electron and photon fluxes into apexes of the surface. This structuring of the solution surface could be standing waves produced by acoustic transducers. NP growth is, to some degree, a threshold process. NP growth requires formation of a critical cluster size which, for PDSE, requires a critical fluence of reducing agents incident onto the surface. Structuring the solution surface could provide locally critically large electron fluences that would aid in NP growth, selectivity and particle size.

In this paper, we discuss results from a computational investigation of PDSE intended for Ag NP synthesis while

using AgNO$_3$ solutions with wavy surfaces, as might be produced by acoustic transducers. The simulations were performed with the 2-dimensional (2D) *nonPDPSIM* modeling platform [28] and the zero-dimensional, plug-flow model, *GlobalKin* [25]. A helium APPJ plasma was incident on flat and structured liquid surfaces of varying wavelength and solution conductivity. Under most operating conditions, formation of Ag NPs by PDSE is controlled by the fluence (time integral of flux) of reducing species onto the surface of the solutions, and electron fluences in particular. We found that the curvature and conductivity of the surface of the solution intensified the electron and VUV photon fluxes to the apexes of the wave patterns. Higher conductivities (as produced by a larger molarity of the AgNO$_3$ solution) and shorter wavelengths of the surface structure produced more intense electron fluences to the apexes of the waves. For low conductivity solutions having long wavelength structures, the ratio of electron fluences to apex of the waves compared to the troughs of the waves was 2–5. For high conductivity solutions and shorter wavelengths this ratio can be several hundred. These spatially controlled electron fluences then produce spatially differentiated formation of Ag NPs.

An overview of the numerical methods, simulation geometry, and chemical reaction mechanism used in this investigation are in section 2. Results are discussed in section 3 for fluid and plasma properties of the base case—a 65 ns, 15 kV discharge sustained in He/O$_2$ onto a flat 5 mM AgNO$_3$. Plasma properties for APPJs incident onto structured AgNO$_3$ solutions are discussed in section 4. The consequences of structuring the liquid surface structure on densities of Ag NP precursors (Ag—Ag$_4$) after a single pulse are discussed in section 5. Trends for NP formation over 100 s of plasma exposure of the solution for electron fluences at apexes and troughs are also discussed. Concluding remarks are in section 6.

2. Description of the models and conditions

The 2D fluid model *nonPDPSIM* was employed in this work to investigate the control afforded by acoustically structured plasma–liquid interfaces as applied to the PDSE of Ag NP. *nonPDPSIM* has been previously described in detail [28], and so a brief overview is provided here.

nonPDPSIM is a multi-fluid simulation employing a 2D unstructured mesh. The simulation begins by solving a modified version of the compressible Navier–Stokes (NS) equations (continuity, momentum, energy) for the neutral flow field resulting from inlet nozzles and pumps. The particular form of the NS equations solved is couched in terms of number densities instead of mass densities to better address large gradients in mass density for conditions that are essentially isobaric. The integration of the NS equations continues throughout the simulation, while accounting for momentum transfer to the neutral fluid from electric field driven ions and electrons.

The electric potential, charged species densities, and material surface charges are obtained using a fully-implicit solution of Poisson's equation which is solved concurrently with changes in charged species densities employing a Newton–Raphson method. Charged species fluxes are obtained using a Scharfetter and Gummel method, while charged and neutral species densities are updated using finite volume based discretization of their continuity equations.

Bulk average electron energy, ε, as a function of position is obtained from an implicit solution of the electron energy conservation equation which is solved using a successive-over-relaxation method. This average energy then defines the effective electron temperature, $\varepsilon = \frac{3}{2} k_B T_e$ (k_B Boltzmann's constant). The electron temperature is updated synchronously with Poisson's equation for electric potential such that it is closely coupled to changes in charged particle densities and surface charges. Electron-impact rate coefficients are obtained from stationary solutions of Boltzmann's equation for the electron energy distribution (EED), solved over a range of reduced electric field (electric field/gas number density, or E/N) values to account for the non-Maxwellian nature of the EEDs. From these solutions, multiple lookup tables of electron-impact rate and electron transport coefficients as a function of effective electron temperature are constructed and assigned to zones within the mesh dependent on the local gas composition. Rate coefficients extracted from the table are interpolated to the effective electron temperature within each simulation cell, which retains information on the non-Maxwellian EEDs.

Secondary electron emission is included with a secondary emission coefficient of 0.1 on all surfaces for all incident positive ion species. Given operation at atmospheric pressure, the temperature of secondary electrons was assumed to be the bulk (fluid) electron temperature within the same cell. Photoemission and photoionization were included, where radiation transport is modelled employing a Green's function. Photoionization was produced by VUV photoemission from excited He(2^{1}P) (58.4 nm), and He$_2^*$ dimer (broadband radiation centered on ≈70 nm). Radiation originating from He(3P) was not included in the model as its intensity is low compared to that originating from He(2^{1}P) and He$_2^*$. Photoionization of gas phase O$_2$ and both gas and liquid phase H$_2$O was included with radiation trapping being addressed as described by Leitz *et al* [11].

In the discussion of results, we refer to the dielectric relaxation time, $\tau = \varepsilon/\sigma$, where ε is the permittivity and σ is the conductivity. τ is a measure of how rapidly accumulated charge will dissipate by electric field driven currents. Larger conductivity produces larger current that removes charge more rapidly and produces a smaller τ. Larger permittivity produces a smaller electric field and lower current density requiring more time to dissipate the charge (a larger τ). Charge dissipation and τ is a natural outcome of the model by simultaneously solving Poisson's equation ($\nabla \cdot \varepsilon \vec{E} = \nabla \cdot \varepsilon \nabla \phi = -\rho$, for electric field E, potential ϕ and charge density ρ) and charge density ($d\rho/dt = -\nabla \cdot \vec{j} = -\nabla \cdot \sigma \vec{E}$).

Transport of gas and liquid phase species within their own phases is given by their diffusion fluxes, or in the case of charged particles, drift-diffusion fluxes using transport coefficients for only that phase. The fluxes of a gas phase species into and out of the liquid are limited by Henry's law

equilibrium at the surface of the liquid. The gas phase flux of a neutral species entering the liquid is

$$
\Gamma_{gl} = \left[\begin{array}{l} \dfrac{D_g}{\Phi x} \Big) 1 \quad \dfrac{n_l}{n_g h} \displaystyle\sum \Big) n_g \quad n_l +; \quad n_l \leqslant n_g h, \\ 0, \quad n_l > n_g h \end{array} \right.
\tag{1}
$$

where n_g is the gas density at the numerical node adjacent to and Φx away from the liquid having gas phase diffusion coefficient D_g. The solvated liquid phase partner of the gas phase species has density n_l at the surface of the liquid. h is the Henry's law equilibrium constant. The flux of the gas phase species into the liquid goes to zero when the solvated species at the surface of the liquid is saturated. The flux of a liquid phase species leaving the liquid into the gas, Γ_{lg} having diffusion coefficient in the liquid D_l is

$$
\Gamma_{lg} = \left[\begin{array}{l} \dfrac{D_l}{\Phi x} \Big) 1 \quad \dfrac{n_g}{n_l/h +} \displaystyle\sum \Big) n_l \quad n_g +; \quad n_g \leqslant n_l \overline{\gamma} h \Big(\\ 0, \quad n_g > n_l \overline{\gamma} h \Big(. \end{array} \right.
\tag{2}
$$

The flux of species leaving the liquid goes to zero when the gas phase is saturated with respect to the liquid concentration at the surface. These transport limits based on being super-saturated, at equilibrium, and sub-saturated applies only to neutral fluxes passing through the gas–liquid interface. The transport of species in the gas phase and in the liquid away from and towards the surface are not otherwise constrained. It was assumed that all ions and photons with fluxes into the gas–liquid interface enter the liquid, although the algorithm allows for an accommodation coefficient to limit the ion flux that enters the liquid.

Electrons incident onto the surface of the solution are immediately converted to solvated electrons, denoted as $e(H_2O)_{aq}$. The temperatures of the liquid phase and of solvated electrons temperatures were held at a constant at 300 K. With the solution functionally serving as the anode, electrons are initially accelerated into the solution prior to its charging. The incident electron flux has energies of several eV. When striking the solution, these electrons can undergo inelastic collisions prior to solvation, resulting in dissociation and ionization of surface resident molecules. These inelastic electron-collisions with the top layer of the liquid are particularly important for plasma–liquid interactions with surfactant molecules which preferentially are found at the surface of the solution [29].

To address the possibility of inelastic collisions of gas phase electrons with the surface of the liquid, the plasma-surfactant module (PSM) was developed for *nonPDPSIM*. Here, the term surfactant is used in the most general manner, and refers to any liquid phase molecule that resides on the surface. For lack of liquid-phase electron-molecule cross sections, we assumed that gas phase cross sections applied to the interaction between the incident gas phase electrons and the liquid surface resident molecules. At the liquid phase mesh point i having neighboring mesh nodes j in the gas phase, the rate of reaction for process m, R_{im} ($cm^{-3}s^{-1}$), resulting from the incident gas phase electron flux is

$$
R_{im} = \left] \sum_{j}^{\text{neighbors}} \dfrac{f_j \Gamma_{ji} M_m}{V_i} \min \Big) \dfrac{k_{jm})T_{e,j} +}{v_{th,j}}, A_s \right. .
\tag{3}
$$

The sum is over gas phase mesh points which are neighbors of liquid node i. $k_{jm}(T_{e,j})$ is the electron-impact rate coefficient at node j for process m, where the electron temperature at the gas phase node is $T_{e,j}$. $v_{th,j}$ is the thermal speed of electrons arriving from node j to node i. The ratio $k_{jm})T_{e,j} + /v_{th,j}$ is an effective cross section for the interaction. $A_s = N^{-2/3}$ is the cross sectional area of a surface site where N is the total liquid phase density. M_m is the mole fraction of the liquid phase species for process m at the surface of the liquid. Γ_{ji} is the electron flux from gas phase node j to liquid phase i passing through the face of the liquid volume element having fractional area f_j. V_i is the volume of the liquid cell. With electron penetration distances of a few to tens of nm (a dimension which is not resolved in the numerical mesh), we assume that all incident electrons react at the surface. The minimum function in equation (3) limits the effective cross section to the area of a surface site occupied by the molecule. An analogous expression is used for reactions of gas phase neutral species with surface resident liquid species.

The products of the electron (or neutral) impact with surface-resident liquid species are assumed to remain in the liquid phase, though the algorithm allows for products to return to the gas phase. This latter process likely occurs for large surfactant molecules whose hydrophobic end penetrates above the surface. Dissociating the hydrophobic end of the molecule likely results in a fraction of the dissociation products entering the gas phase. However, in this investigation, the only surfactant molecule is water itself.

Gas phase electron-impact cross sections for H_2O were used for the liquid phase, resulting in production of $H_2O^+{}_{aq}$, $e(H_2O)_{aq}$, OH_{aq}, and H_{aq}. We assume that the electron produced in the incident gas phase electron ionizing the surface resident water is then immediately solvated. Due to the manner in which the PSM was implemented, computationally this was accomplished by producing an intermediate non-solvated electron in the liquid which then rapidly solvated.

PDSE processes to produce, for example, NPs using DC and pulsed plasma sources operating at many to tens of kHz may take many seconds to a few minutes to complete. This elapsed time and number of pulses is beyond what can be addressed using the 2D model. To evaluate the consequences of the different electron fluences onto solutions that may result from having structured surfaces, the model *GlobalKin* was used [25]. *GlobalKin* is a zero-dimensional (plug-flow) plasma kinetics and plasma chemistry modeling platform capable of addressing plasma–liquid interactions. *GlobalKin* was used in our prior investigation of plasma jet treatment of $AgNO_3$ solutions for production of Ag NPs [25].

Although *GlobalKin* is capable of addressing coupled plasma–liquid interactions simultaneously with in-solution chemistry, only the in-solution plasma-activated chemistry capabilities were used here. Electron and ion fluences onto the surface of $AgNO_3$ solutions as a function of location on

the surface were computed with *nonPDPSIM* over a single pulse. These fluences were converted to time averaged fluxes by specifying a pulsed repetition frequency (PRF). The electron temperature above the solution surface during delivery of the fluxes computed by *nonPDPSIM* was also recorded. These values were then used in *GlobalKin* as the fluxes incident onto the surface of the solution. The same algorithms used in *nonPDPSIM* for interactions between gas phase species and surface resident species in solution (the PSM) were also incorporated into *GlobalKin*. Additional cases were run with *GlobalKin* to represent solution chemistry resulting from fluences incident on different locations on the surface over long periods of time.

The source geometry used in this work is shown in figure 1(a). The 2D Cartesian geometry implemented in *nonPDPSIM* is symmetric about the left-hand boundary. The APPJ is patterned after that used in experiments by Jiang and Bruggeman [31]. The APPJ was positioned above a glass dish containing the liquid. The APPJ source consists of a tungsten powered electrode 1 mm in diameter situated inside a 2.0 mm inner diameter, 0.7 mm thick glass tube (relative permittivity $\varepsilon_r = 4.5$). The inner tube is coaxial to a 9.5 mm inside diameter, 1.6 mm thick outer glass tube ($\varepsilon_r = 4$). The downstream end of the powered electrode and both glass tubes are terminated in rounded tips. A 1.2 cm radius glass dish ($\varepsilon_r = 4$) was positioned downstream of the source. The dish contains water to a height of 0.8 mm, for a total liquid volume of 9.6 ml. The distance from the tip of the electrode to the surface of the flat liquid is 10 mm. A 5.4 mm tall, 0.88 mm wide metal ring is positioned coaxially around the inner tube centered at a height of 1.3 cm. This metal ring can function as a grounded electrode, but remained electrically floating in this work. As such, the path to ground from the powered electrode proceeds through the liquid and glass dish to the grounded metal foil under the dish resulting in the discharge directly impinging on the liquid surface below the source aperture.

The flat liquid mesh nodes and connectors are shown in figure 1(b) where the mesh resolution varies between a minimum of 0.04 mm/cell across the plasma–liquid interface and a maximum resolution of 1.0 mm/cell in the ambient air to the right of the source. The numerical mesh used for the flat liquid consists of 14 143 total nodes, comprising 8372 gas-phase nodes and 2526 liquid-phase nodes. These numbers vary less than 20% over all the acoustically structured liquid surface meshes.

The results discussed here are sensitive to the shape of the mesh at the interface between the gas and liquid phases. With the permittivity of the solution being large ($\varepsilon_r = 80$) and conductivity typically being small, the surface of the liquid charges negatively in proportion to the local capacitance (C [F cm^{-2}]). The large permittivity results in electric field enhancement in the gas phase above the liquid, which is then augmented by surface charging which produces a sheath. The magnitude of the electric field at the first gas phase mesh point above the liquid is sensitive to the physical distance, Φx_g, of that mesh point from the liquid measured parallel to the surface normal. Smaller Φx_g results in a larger electric field at that mesh point. Charging of the liquid surface is in turn sensitive to
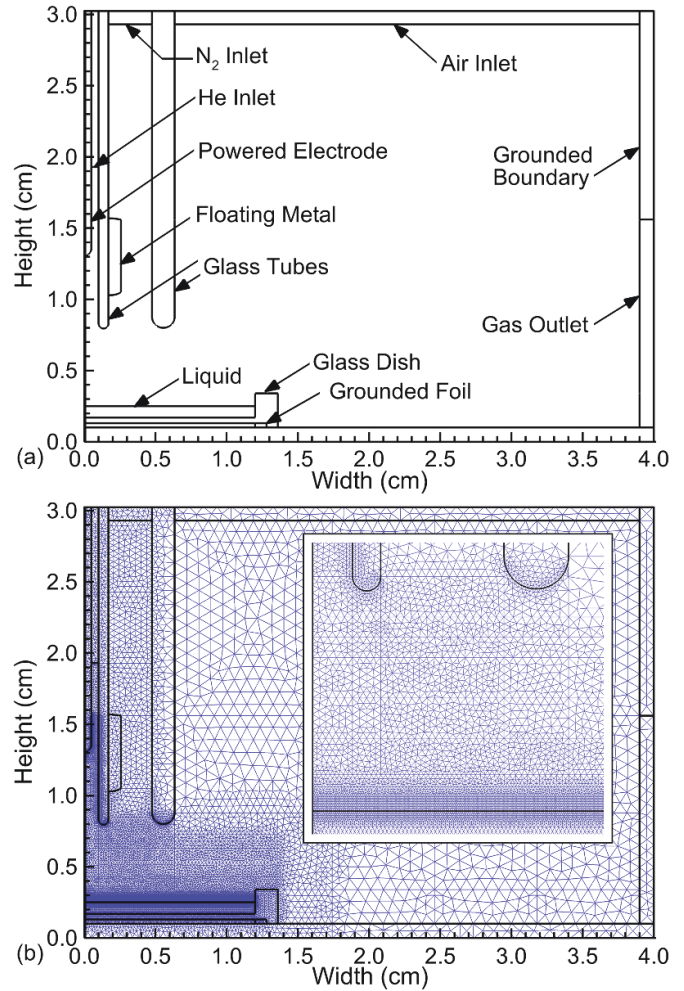

Figure 1. Schematics of the (a) APPJ geometry and (b) the flat ($n00$) liquid surface mesh. (Figure (a) reprinted from [30], with the permission of AIP Publishing.)

the physical distance, Φx_l, of the first mesh point below surface along the inverse normal to the surface. This sensitivity results from the local capacitance C being inversely proportional to Φx_l. If the values of Φx_g and Φx_l are allowed to randomly vary along the surface about a mean value, as may occur if mesh generators are not otherwise constrained, the densities of electron-impact generated species above the surface, their fluxes onto the surface, and surface charging will be numerically noisy. This noise can be significantly reduced by having several layers of numerical mesh points, both in the gas phase and in the liquid, that are parallel to the liquid surface. This best practice extends to any dielectric material in contact with the plasma.

All cases employed a flow of 1 slm He/O$_2$ = 0.995/0.005, supplied through the central inlet at the top of the inner glass tube with 30 ppm humid air impurity. A 2.5 slm N$_2$/H$_2$O = 0.995/0.005 nitrogen shroud flow entered through the outer co-axial inlet. The region beyond the source and dish was initiated as humid air. A 10 slm flow of humid air (N$_2$/O$_2$/H$_2$O = 0.795/0.2/0.005) entered through the top

Table 1. Species in the reaction mechanism used in *nonPDPSIM*.

Gas phase charged	e, H^+, H^-, H_2^+, H_3^+, OH^+, OH^-, H_2O^+, H_3O^+, O^+, O^-, O_2^+, O_2^-, O_3^-, N^+, N_2^+, N_3^+, N_4^+, NO^+, NO_2^+, NO_2^-, NO_3^-, NH^+, He^+, He_2^+, HeH^+
Gas phase neutral (ground states)	He, H, H_2, OH, H_2O, HO_2, H_2O_2, O, O_2, O_3, N, N_2, NO, NO_2, NO_3, N_2O, N_2O_3, N_2O_4, N_2O_5, HNO, HNO_2, HNO_3, HNO_4
Gas phase neutral (excited states)	H^*, H_2^*, O^*, O_2^*, O_2^{**}, $O_2(v)$, N^*, N_2^*, N_2^{**}, $N_2(v)$, OH^*, $He(2s^3S)$, $He(2s^1S)$, $He(2p^3P)$, $He(2p^1P)$, $He(3s^3S)$, $He(3p^3P)$, He_2^*
Liquid species	H_2O_{aq}, $e(H_2O)_{aq}$, $H_2O^+_{aq}$, $H_3O^+_{aq}$, H_2O_{2aq}, HO_{2aq}, OH_{aq}, OH^+_{aq}, OH^-_{aq}, H_{aq}, H_{2aq}, O_{aq}, O_{2aq}, $O_2^+_{aq}$, O_{3aq}, O^-_{aq}, $O_2^-_{aq}$, $O_3^-_{aq}$, $HO_2^-_{aq}$, NO_{aq}, NO_{2aq}, NO_{3aq}, N_2O_{3aq}, N_2O_{5aq}, $NO_2^-_{aq}$, $NO_3^-_{aq}$, $NO_4^-_{aq}$, $ONOO^-_{aq}$, HNO_{aq}, HNO_{2aq}, HNO_{3aq}, HNO_{4aq}, $ONOOH_{aq}$, N_2O_{aq}, $NO_2^+_{aq}$, N_{aq}, N_{2aq}, NO^+_{aq}, He_{aq}
Silver species	Ag_{aq}, Ag^+_{aq}, Ag^{2+}_{aq}, Ag_{2aq}, $Ag_2^+_{aq}$, $Ag_2^{2+}_{aq}$, $Ag_2^{3+}_{aq}$, Ag_{3aq}, $Ag_3^+_{aq}$, $Ag_3^{2+}_{aq}$, $Ag_3^{3+}_{aq}$, Ag_{4aq}, $Ag_4^+_{aq}$, $Ag_4^{2+}_{aq}$, $Ag_4^{3+}_{aq}$, $AgOH^+_{aq}$, $AgNO_{3aq}$

boundary of the computational domain to minimize artificially large vortexing resulting from the differential flow velocity tangential to the lip of the glass dish. To emulate evaporation of the solution into the ambient, the gas phase density of H_2O at the liquid interface was held constant at a value corresponding to the vapor pressure of water at 1 atm and room temperature, a partial pressure of 18 Torr. An initial 15 ms of neutral fluid simulation was performed prior to each plasma simulation to obtain a converged fluid flow field and to establish an equilibrium saturated water vapor layer above the liquid surface. This was accomplished by initiating the entire gas phase with the He/O_2 gas mixture and then turning on the shroud and humid air flows. The base case employed a single 15 kV, 47.5 ns flat-top pulse with a 2.5 ns rise time and 15 ns fall time.

The gas and liquid reaction mechanism used in *nonPDP-SIM* consisted of 25 charged species, 23 neutral species, and 18 excited states in the gas phase; 39 non-silver liquid species, and 17 silver-containing liquid species, listed in table 1, with a total of 2179 reactions. (The subscript aq denotes an aqueous or in-solution species.) The air reaction mechanism was based on Van Gaens and Bogaerts [32], and helium reactions were included by Norberg *et al* [33] and Emmert *et al* [34]. Non-silver liquid-phase reactions were employed as described in Tian and Kushner [35], with additions from Lietz and Kushner [36] and Meyer *et al* [37]. Additional reactions were added and treated with the surfactant module. These reactions include dissociation, dissociative attachment, and ionization of H_2O_{aq}, based on the data for gas phase reactions [38].

The liquid-phase silver reaction mechanism was developed by Raisanen *et al* [25]. The full mechanism considers silver species of Ag_n^{m+} where $n = 1$–9 and $m = 0$–3 cation charge states. This mechanism was developed to investigate PDSE of $AgNO_3$ for the synthesis of NPs. The dominant process in formation of NPs is the reduction of Ag_n^{m+} cations by solvated electrons (denoted as $e(H_2O)_{aq}$ in table 1),

$$e(H_2O)_{aq} + Ag_n^{m+} \rightarrow Ag_n^{(m-1)+} + H_2O \quad (4)$$

The formation of neutral Ag_n initiates or sustains a cascade producing larger Ag_n^{m+} clusters. In this mechanism, Ag_n^{m+} species having $n > 9$ were classified as NPs Ag(NP), whose

average properties (mass, diameter) are calculated as a function of time. NP species having charge states $m = 0$–3 were included.

In [25], the mechanism was employed in investigations using a global plug-flow model over several seconds which enabled nearly full reduction of $AgNO_3$ solutions of several to tens of mM. This full mechanism was used for simulations using *GlobalKin*. In addition to the processes described in [25], the consequences of Ostwald ripening [39] were included in the mechanism. Ostwald ripening is a process that effectively limits the size of NPs that are produced in solution chemistry. Based on experiments by others for expected sizes of NPs for our conditions [1], we included Ostwald ripening by limiting the rate coefficient for agglomeration between NPs. The limited rate coefficient, k_{lim}, for agglomeration between species classified as NPs having radii r_1 and r_2, is

$$k_{lim} = k_0 \times \exp \left(-r_{lim}^2 \left/ \left(\frac{1}{2} \right) r_1 + r_2 \right. \right) \quad (5)$$

where k_0 is the unlimited rate coefficient and r_{lim} is the limiting radius. Here, we used $r_{lim} = 10$ nm. Growth of NP to radii greater than r_{lim} occurs by adding smaller atoms and clusters through surface growth.

In simulations using *nonPDPSIM*, single discharge pulses onto $AgNO_3$ solutions were investigated having electron fluences onto the solution that are not large enough to fully reduce the Ag_n^{m+}, and so the densities of large clusters approaching NPs following the single pulse are negligible. In recognition of these trends and to reduce the computational burden, only Ag_n^{m+} with $n \leqslant 4$ were included in the reaction mechanism for *nonPDPSIM*. Plasmas onto solutions of $AgNO_3$ having molarities between 1 mM to 50 mM were investigated.

This work addresses acoustic shaping of a plasma treated liquid surface, its impact on particle transport across the plasma–liquid interface, and the corresponding control that may be achieved over the reduction and nucleation of silver NP precursor species and NP production. The acoustically structured liquid surfaces are shown in figure 2. The liquid surface structures are sinusoidal in shape, described by their wavelength, λ, and peak-to-peak amplitude, A_{pp}. Wave structures will be referred to by their wavenumber, *nxx*, where *xx* refers to the total number of complete wavelengths across the
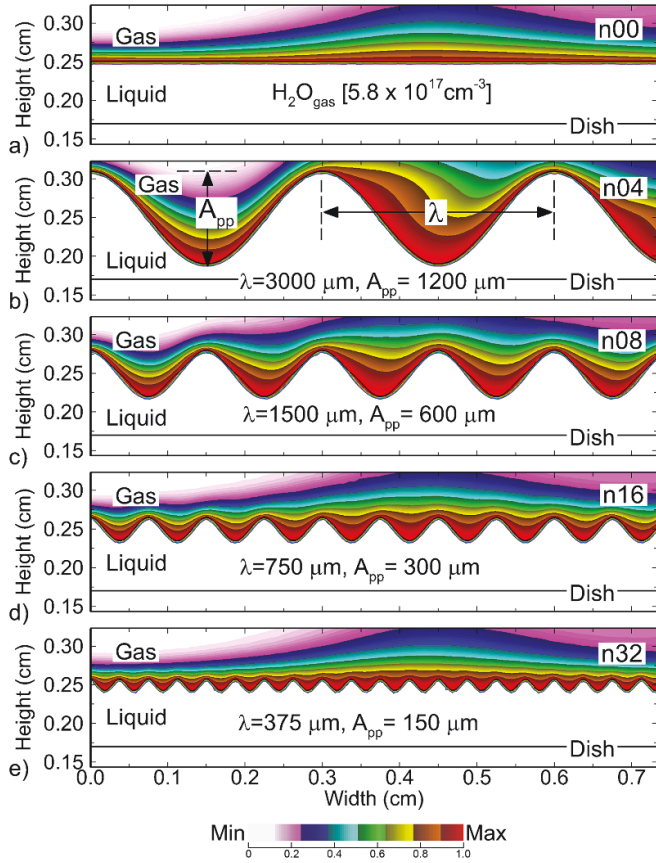
Figure 2. Schematics of the acoustically structured liquid surfaces. *nxx* refers to the number of wavelengths contained across the dish. λ is the wavelength of the structures and A_{pp} is the peak-to-peak amplitude. (a) *n*00, (b) *n*04, (c) *n*08, (d) *n*16, and (d) *n*32. The flood contours show the H_2O vapor density resulting from evaporation of the solution on a linear scale with maximum value 5.8×10^{17} cm^{-3}.

1.2 cm dish half-width. In addition to the flat control case, four structured surfaces were investigated with wavenumbers of *n*04, *n*08, *n*16, and *n*32, corresponding to acoustic driving frequencies of 100 Hz, 200 Hz, 500 Hz, and 1500 Hz. These values were chosen to closely match experimentally obtained limits for the highest possible (Rayleigh instability limited) amplitude for each wavelength. Wavenumbers of *n*04, *n*08, *n*16, and *n*32 have wavelengths of 3000 μm, 1500 μm, 750 μm, and 375 μm with peak-to-peak amplitudes of 1200 μm, 600 μm, 300 μm, and 150 μm. The average heights of the structured surfaces were the same as for the flat surface. The maximum height of each surface was aligned on-axis (width $=$ 0.0 cm) to enable continuity across the symmetric left boundary. Consequently, the distance between the powered electrode and the liquid surface on axis was smaller by half the peak-to-peak amplitude of each structured case relative to the flat case.

For the Cartesian geometry employed here, the structured surfaces are effectively a series of parallel waves, rather than concentric rings as would be the case in cylindrical geometry. The wavy surfaces have larger area (and larger length along the surface) compared to the flat base-case. For a sinusoidal

surface, the effective length L along the surface for a single wavelength is a factor of 1.216 greater than the linear distance between the start and end points below the curve.

3. APPJ onto a flat liquid surface

As a point of comparison for pulsed APPJs incident onto structured liquid surfaces, the plasma properties of an APPJ onto a flat liquid surface (*n*00) was first investigated. The initial gas flow fields for He, N_2, O_2, and H_2O prior to pulsing the discharge are shown in figure 3. For this baseline case, and all cases that follow, 1 slm of He/$O_2 =$ 99.5/0.5 with 30 ppm humid air impurity was flowed through the inner tube. 2.5 slm of N_2 with 0.05% H_2O was supplied through the outer tube. A background flow of 10 slm of humid air ($N_2/O_2/H_2O =$ 79.5/20/0.5) was supplied from the top boundary (not shown).

The volume below the powered electrode and a 0.5 cm wide region adjacent to the liquid surface consist of a relatively homogeneous He gas. The N_2 shroud confines the He due to the short residence time and low rate of diffusion of He into the N_2. The radial He flow velocity varies between 500 and 2000 cm s^{-1} across the liquid surface, reaching a maximum of 3400 cm s^{-1} as it is compressed crossing the lip of the glass dish at a width of 1.2 cm. The He flow only moderately mixes into the N_2 shroud. The N_2 flow is effective in isolating the ambient gases from the He flow with there being little penetration of O_2 from the ambient into the He. Water vapor evaporates from the liquid surface with a density at the surface of $5.8 \sim 10^{17}$ cm^{-3} corresponding to the saturated vapor pressure at 300 K. The high He and N_2 flow velocities over the surface of the liquid entrain the water vapor, resulting in an inhomogeneous distribution of water vapor across the liquid surface. The water vapor is compressed where the He and N_2 intersect the liquid surface. Water vapor accumulates in the stagnation zone at the lip of the dish.

The electron density and ionization source close to the liquid surface are shown in figure 4 during a 65 ns, -15 kV pulse rising from 0 kV to -15 kV over the first 2.5 ns, maintaining a flat-top until 50 ns. The solution contains 5 mM of $AgNO_3$ whose conductivity is approximately 0.5 mS cm^{-1}. The discharge is initiated with a neutral spot of plasma placed at the tip of the electrode having density of 10^{11} cm^{-3} and diameter of 500 μm. Between 0 and 19 ns, a Townsend ionization wave (IW) propagates from the powered electrode towards the liquid surface. The initial forward IW is accelerated through an E/N of $\approx$120 Td (1 Td $= 10^{-17}$ V cm^2), resulting in a maximum electron temperature of 8.5 eV in the front of the IW. Although the solution is conductive, its dielectric relaxation time ($\tau = 15$ ns) is commensurate with the length of the discharge pulse. As a result, the surface of the solution charges negatively, producing parallel components of the electric field to launch a SIW. From 20 to 40 ns the discharge propagates across the liquid surface with the maximum electron density reaching $2 \sim 10^{15}$ cm^{-3}, as shown in figure 4(a). The speed across the surface of the SIW is $-3 \sim 10^7$ cm s^{-1}.
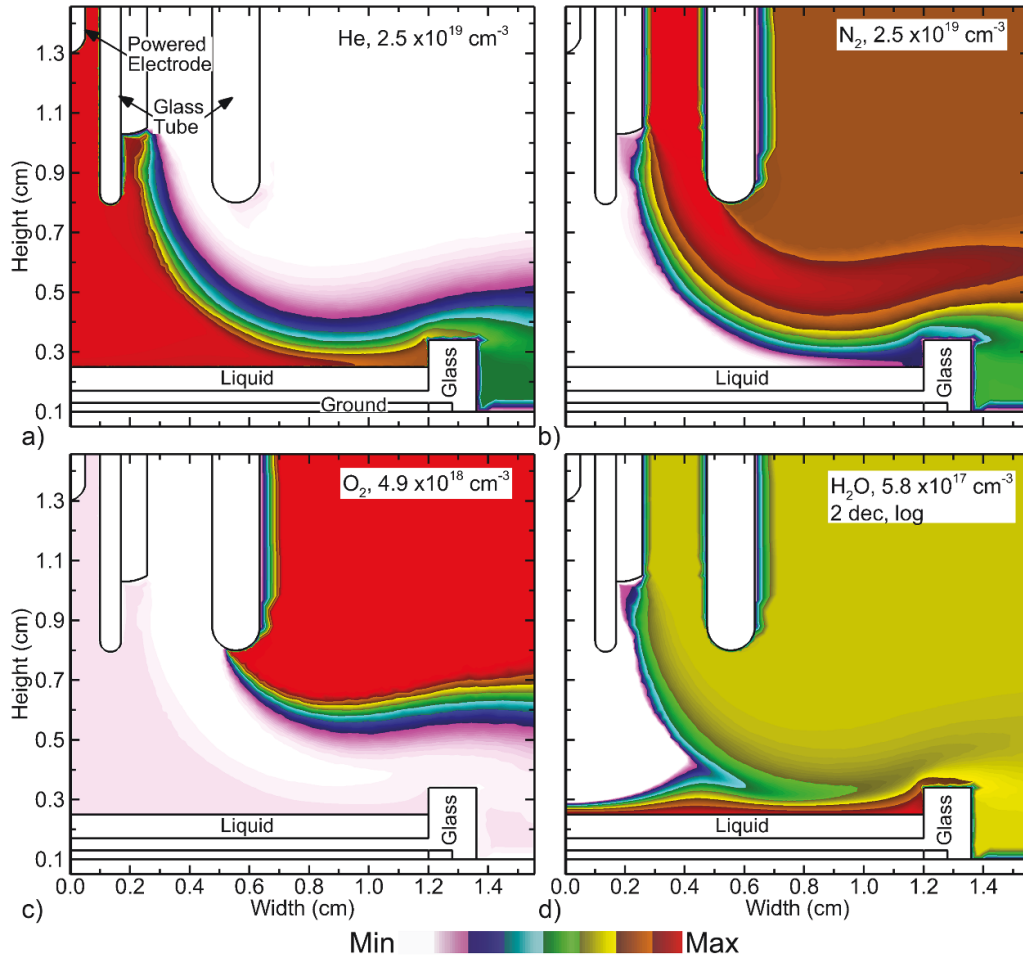
Figure 3. Initial neutral densities prior to pulsing the APPJ for the flat liquid surface. (a) Helium, (b) nitrogen, (c) oxygen, and (d) water vapor. Operating conditions: 1 slm of He/O_2 = 99.5/0.5 with 30 ppm humid air, 2.5 slm of N_2 with 0.05% water vapor, and 10 slm humid air ($N_2/O_2/H_2O$ = 79.5/20/0.5) through the inner, outer, and atmospheric boundary inlets, respectively.

The electron-impact ionization source S_e shown in in figure 4(b) has distinct regions being net positive and net negative, the latter indicating that attachment and recombination dominates over ionization. (The absolute value of the ionization source S_e is plotted in figure 4(b). The regions of net positive ionization and net loss are labeled with '/' and ' '.) The head of the SIW has a positive ionization source exceeding $1 \sim 10^{24}$ cm^{-3} s^{-1}. With passage of the head of the SIW, the trailing liquid surface has been charged akin to a solid dielectric. With the SIW propagating through the saturated water vapor boundary layer, the S_e transitions to being negative. The rate of electron losses by dissociative recombination of H_2O^+ and H_3O^+ and dissociative attachment to H_2O are rapid compared to losses in the bulk helium. Electron-impact ionization sources remain positive above the H_2O dominated boundary layer.

The ionization source not involving electron-impact processes, S_{all}, shown in figure 4(c), has a maximum value of $2 \sim 10^{23}$ cm^{-3} s^{-1}. In the gas phase, S_{all} consists of dominantly Penning ionization with small contributions from photoionization. On the surface of the liquid layer, photoionization is the dominant source of ionization.

The propagation of SIWs across a surface, solid or liquid, can be explained in part by current continuity. Consider a geometry similar to that investigated here, consisting of a sequence of series impedances—a powered electrode, gas gap, liquid, dielectric dish, and ground plane. Current continuity must be maintained through this series of impedances. An IW begins from the powered electrode directed towards the surface. Current in the ionized column behind the head of the IW is in large part conduction current. Current continuity ahead of the IW wave in the non-conductive gas is maintained by displacement current. Assuming the liquid is poorly conducting, current through the liquid (and underlying dielectric dish) is displacement current, terminating as conduction current at the grounded electrode. When the conductive plasma channel reaches the liquid, the surface of the liquid initially charges, which is equivalent to charging the series capacitances of the liquid and underlying dish. When this capacitance has been fully charged, displacement current can no longer flow through that location on the liquid surface. To maintain current continuity, the plasma expands as a SIW onto uncharged liquid, which then enables displacement current to flow through that locally uncharged capacitance.
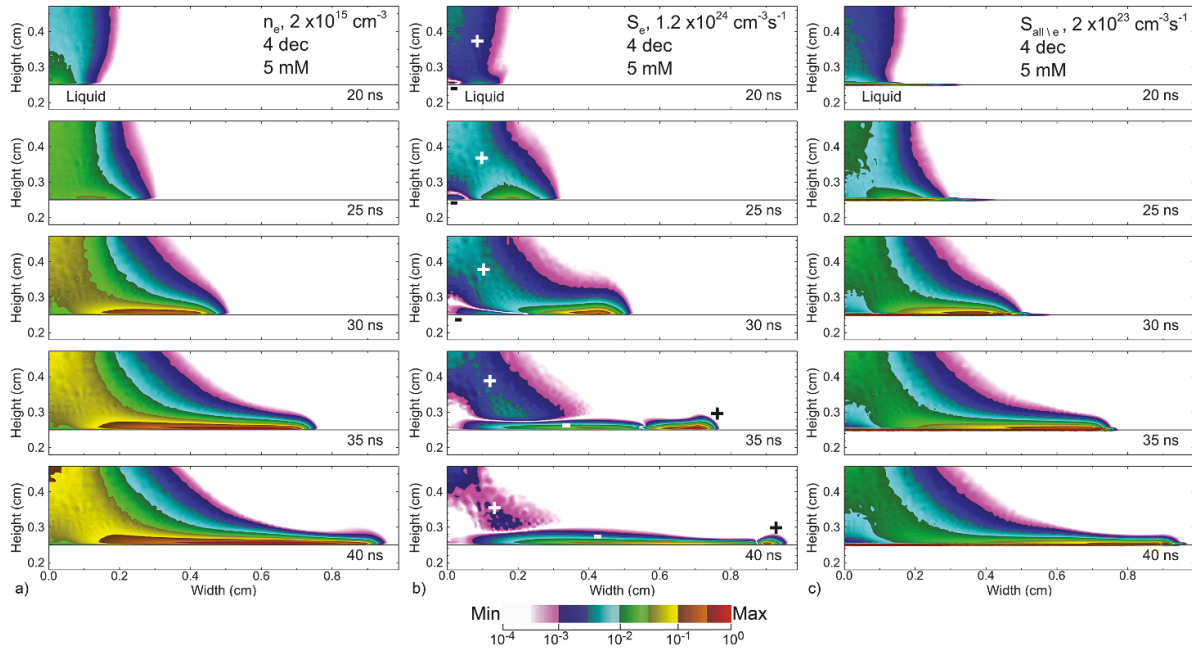
Figure 4. Macroscopic plasma properties for the APPJ incident onto the flat (*n*00) liquid surface (5 mM AgNO₃ solution). (a) Electron density, (b) electron-impact ionization source, and (c) ionization source due to processes other than electron-impact. Operating conditions are 15 kV, 47.5 ns flat top pulse with 2.5 ns rise and 15 ns fall, 1 slm He/O₂ = 99.5/0.5 within 2.5 slm N₂ shroud gas. Values are plotted on 4-decade log scales with maximum value noted. The absolute value of the electron-impact ionization source is plotted. The portions of the image labeled '+' and ' ' indicate regions of net electron source and loss.

As the conductivity of the liquid increases, current continuity can be maintained increasingly as conduction current through the liquid. As such, there is less need for the plasma to expand as a SIW, seeking out uncharged surface to pass displacement current. A more conductive liquid is also less able to support horizontal components of the electric field that enable propagation of the SIW. In the limit of metal-like conductivities, there would be no requirement for the plasma to expand as a SIW for current continuity to be maintained as the current can be conducted directly through the solution.

This trend of less expansive SIWs on the surfaces of solutions with increasing conductivity is demonstrated in figure 5, where electron densities are shown at 40 ns for solution molarities of 0 mM (essentially pure water) to 50 mM. The conductivities of the AgNO₃ solutions vary from 0.1 mS cm⁻¹ for the 1 mM solution to 5 mS cm⁻¹ for the 50 mM solution. With pure water (0 mM solution), the liquid is functionally a dielectric and passes only displacement current. The local charging of the surface of the liquid in large part terminates passing displacement current into the liquid. The discharge then proceeds as a detached SIW. (Recall that following propagation of the SIW, the electron-impact ionization source in the water vapor dominated boundary layer is negative, thereby decreasing electron density behind the head of the SIW). With increasing molarity of the solution and conductivity, current is progressively carried through the liquid as conduction current, resulting in less expansion of the plasma as a SIW along the surface of the liquid.

These trends of decreasing speed of the SIW with increasing conductivity agree with the recent experiments of Herrmann *et al* [40] who observed optical emission from SIWs

propagating across potassium chloride (KCl) solutions in an air ambient. Although their results were made more complex by the onset of filamentation, between a solution having a conductivity of 2 μs cm⁻¹ and a solution having a conductive of 1 mS cm⁻¹, the propagation speed decreased by about 35%.

Recording the extent of the SIW propagation at 40 ns in figure 5 was chosen because the SIWs on the low conductivity solutions strike the wall of the dish prior to the end of the discharge pulse, whereas the SIWs on higher conductivity solutions have nearly reached their maximum extent. For example, the SIWs on the 0, 1 and 5 mM solutions strike the dish by 65 ns. The SIW on the 25 mM solution propagates only 0.08 cm further from 40 ns to 65 ns, and 0.06 cm further on the 50 mM solution.

In this particular geometry, the solution sits in a dielectric dish which represents a series capacitance through which current is carried by displacement current. The current flows through the series impedance of the solution and the underlying dielectric dish. The surface that charges will be that have the largest impedance (smallest capacitance and conductivity). For example, we examine the charge density at the surface of the solution and the surface of the underlying dielectric dish at 40 ns at a position of 0.2 cm. For the discharge onto pure water (0 mM), the liquid surface charges to 2.4 ∼ 10⁻⁵ C cm⁻³ (1.5 ∼ 10¹⁴ q cm⁻³, q ⌉ elementary charge). The underlying dielectric charges to 3.5 ∼ 10⁻¹⁰ C cm⁻³ (2.2 ∼ 10⁹ q cm⁻³). The non-zero charging of the dielectric results from the water having an initial pH of 7, and so there is some intrinsic conductivity. For the discharge onto the 50 mM solution, the roles reverse. The liquid surface charges to 2.6 ∼ 10⁻⁶ C cm⁻³
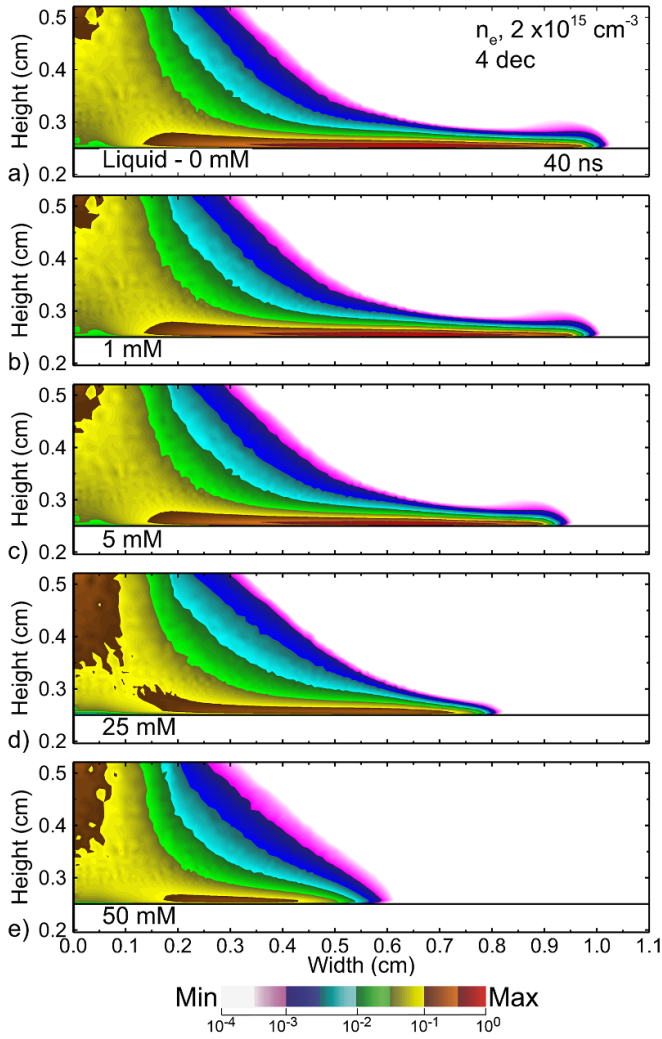
Figure 5. Electron density at 40 ns for the APPJ incident onto the flat (*n*00) liquid surface for different molarity of the AgNO$_3$ solution. (a) 0 mM, (b) 1 mM, (c) 5 mM, (d) 25 mM, (e) 50 mM. The electron density is plotted on a 4-decade log scale. (Figures (a), (c) and (e) reprinted from [30], with the permission of AIP Publishing.)
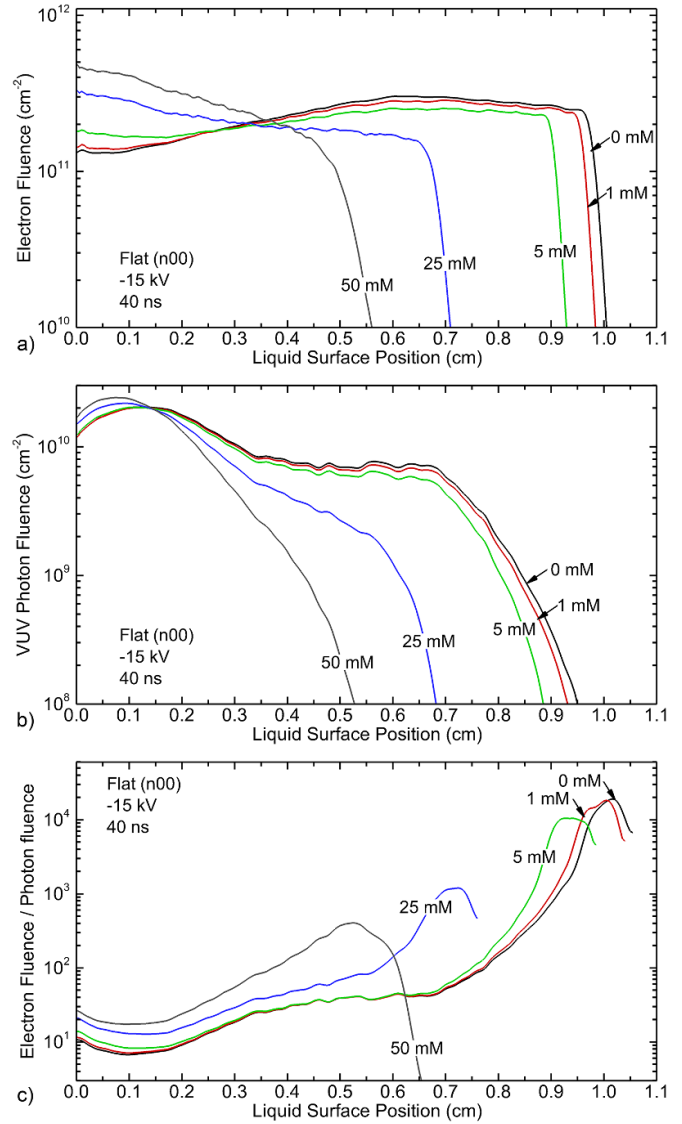

Figure 6. Fluences across the flat (*n*00) liquid surface at 40 ns for varying AgNO$_3$ molarity for a 15 kV pulse. (a) Electron fluence, (b) VUV photon fluence, and (c) ratio of electron to photon fluence. (Figures (a) and (b) reprinted from [30], with the permission of AIP Publishing.)

($1.6 \sim 10^{13}$ q cm^{-3}). The underlying dielectric charges to $1.4 \sim 10^{-5}$ C cm^{-3} ($9.0 \sim 10^{13}$ q cm^{-3}).

The maximum total reduction of Ag$_n^{m+}$ species in solution depends, to first order, on the total available inventory of solvated electrons. The major sources of solvated electrons are gas phase electrons incident onto the surface of the solution, and electrons produced *in-situ* by VUV photoionization of the water. With the absorption length of ionizing VUV photons being only tens of nm, the photo-generated electrons appear to be a surface source of solvated electrons, similar to those produced by the incident electron flux. The availability of solvated electrons for reduction of Ag$_n^{m+}$ is then proportional to the fluence (time integral of flux) of incident electrons and VUV photons. These electron and VUV fluences are shown in figure 6 at 40 ns.

Electron fluences to the solution (figure 6(a)) for the single pulse up to 40 ns have maximum values of $3–6 \sim 10^{11}$ cm^{-2}.

Low AgNO$_3$ molarity (less than a few mM) for a fixed applied voltage results in wider, more uniform electron fluences across the liquid surface. This trend arises due to the low conductivity of the solution, whose capacitance quickly charges and promotes propagation of the SIW. Larger molarity and higher conductivity solutions inhibit propagation of the SIW while focusing electron current into the solution on axis. If the electron mediated processes in the solution were strictly linear with electron fluence, then the area integrated fluence (or inventory) of electrons onto the surface would determine the total amount of reactivity produced by the plasma in the solution. For these conditions, at the end of the voltage pulse, the inventory of electrons onto the solution decreases with increasing conductivity, by a factor of 1.5 from pure water to the 50 mM solution.
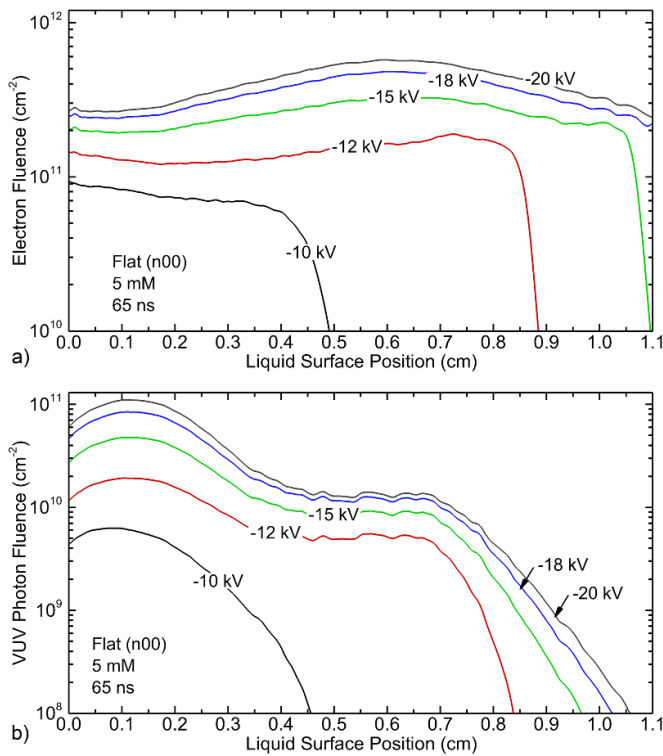
Figure 7. Fluences of (a) electrons and (b) VUV photons across the liquid surface at 65 ns for varying applied voltages and 5 mM AgNO$_3$ molarity.

Through photoionization of liquid water, VUV fluence onto the surface of the solution produces solvated electrons which contribute to reduction of Ag$_n^{m+}$. The VUV fluences onto the solution are shown in figure 6(b) for different AgNO$_3$ molarities. Similar, though less dramatic trends, occur for the VUV fluences compared to the electron fluence. Higher molarity has more concentrated VUV fluences on axis. The VUV fluences are less sensitive to molarity due to the non-local source of the VUV photons. The electron fluence onto the surface originates from electrons a few mean free paths from the surface, which at atmospheric pressure is about 5 μm. The VUV photons from He$_2^*$ emission have mean free paths of many mm and arrive on the surface of the solution from remote locations. The on-axis maximum in VUV fluence for all molarities originates from the common first-strike of the IW onto the surface of the solution which occurs on-axis. Due to the non-local delivery of photons to the liquid surface, the inventory of VUV photons onto the surface is less sensitive to conductivity. The VUV inventory decreases with increasing conductivity by a factor of 1.3 from pure water to the 50 mM solution.

In the specific case of PDSE of AgNO$_3$ solutions for NP synthesis, the primary driver is likely solvated electrons. As such, the source of the solvated electrons—VUV photoionization or direct electron fluxes—may be of secondary importance. However, in chemistries in which different products are generated by VUV and electron fluences, controlling the ratio of these fluences may be important. The ratios of electron-to-VUV fluences for different molarities are shown in figure 6(c). Electron fluences dominate over VUV fluences by a ratio

of 10–25 on axis from pure water to 50 mM solution. Low molarity solutions have significantly larger dynamic range of this ratio. Electron fluences dominate by a factor of 10^3 – 10^4 for low conductivity solutions at larger widths.

The decrease in the VUV fluence (relative to the electron fluence) at large lateral positions is a consequence of the manner of propagation of the discharge and of the SIW. As the discharge progresses and propagates further along the surface, the plasma is increasingly contained within the water dominated boundary layer. For the 5 mM solution on axis 0.5 mm above the liquid, the dominate ions at 40 ns are He$^+$, He$_2^+$ and O$_2^+$. The VUV radiating species (He$_2^*$, He(2^{1}P)) have densities exceeding $2 \sim 10^{13}$ cm^{-3}. At the leading edge of the SIW which is embedded in the water dominated boundary layer, the dominant ions are H$_2$O$^+$ and H$_3$O$^+$, with the VUV radiating species having densities of less than $3 \sim 10^{12}$ cm^{-3}. Integrated over the dwell time of the SIW across the surface then produces progressively smaller fluences of photons compared to electrons.

The just discussed trends on consequences of SIW propagation on conductivity of the solution was focused on the conductivity of the solution as determined by the initial molarity (concentration) of the AgNO$_3$ that is dissolved into the water. Upon solvation, the AgNO$_3$ produces Ag$^+_{aq}$ and NO$_3^-$$_{aq}$. During long term plasma exposure, the conductivity of the solution can change. There could be a decrease in conductivity due to reduction of Ag$_n^{m+}$$_{aq}$ or the formation of higher mass Ag clusters. At the same time, over long periods of processing, the conductivity of the solution can increase due to solvation (and hydrolysis) of, for example, HNO$_3$ which produces H$_3$O$^+$$_{aq}$ and NO$_3^-$$_{aq}$ in solution. Observations of decreasing pH and increasing conductivity of air plasma treated water have been made in several experiments [41]. In these single-pulse simulations, the change in conductivity due to plasma exposure during the discharge pulse is not large. For example, for the 5 mM solution, the maximum decrease in conductivity at the surface of the liquid at the end of the discharge pulse is 1.6% and after 2 μs is 7%. The majority of this decrease in conductivity is not directly due to reduction. The change in conductivity is largely due to reduction of Ag$^+_{aq}$ that initiates formation of heavier mass clusters of Ag$_n^{m+}$$_{aq}$. The conductivity decreases due to there being clusters having smaller ratios of charge-to-mass. This change in conductivity of the surface layer would be significantly smaller after several hundred microseconds or ms of interpulse period due to mixing of the surface layer with the bulk solution.

Increasing the applied voltage increases both the uniformity and the maximum extent of the SIW on the solution. Electron and VUV fluences are shown onto the 5 mM solution in figure 7 at 65 ns (end of the voltage pulse) for voltages of 10 kV to 20 kV. The electron fluence on axis increases from $9.2 \sim 10^{10}$ cm^{-2} at 10 kV to $2.7 \sim 10^{11}$ cm^{-2} at 20 kV, a factor of 3 increase for a factor of 4 increase in stored energy. The maximum fluences at any location increase from $9.2 \sim 10^{10}$ cm^{-2} at 10 kV to $5.6 \sim 10^{11}$ cm^{-2} at 20 kV.

Increasing voltage extends the SIW over the surface of the solution, producing a large disparity in electron fluences. This

disparity is in part a consequence of pulse length and partly a consequence of the finite size of the dish holding the solution. At 10 kV, the bulk IW from the gas phase strikes the surface of the solution at 37 ns, which allows only an additional 28 ns for propagation of the SIW before voltage is terminated. The bulk IW strikes the solution at 19 ns at 15 kV and at 12 ns for 20 kV. With a constant voltage pulse length, the higher voltages simply have a longer time for the SIW to propagate across the surface of the liquid. The extent of propagation of the SIW during the 65 ns voltage pulse is indicated by the location where the electron fluence cascades towards zero. This location is 0.48 cm for 10 kV, 0.88 cm for 12 kV, and 1.1 cm for 15 kV. For larger voltages, the SIW propagates across the entire width of the solution and over the lip of the dish.

The VUV photon fluences onto the solution as a function of voltage show similar trends as the electron fluences. The VUV photon fluence decreases with propagation distance more rapidly than the electron fluence due to the SIW being embedded in the water dominated boundary layer. There are fewer VUV radiating species being produced and those species that are produced are quenched more rapidly by collisions with the water vapor.

4. APPJs onto acoustically structured liquid surfaces

In prior work, the consequences of shaped, wavy solid dielectrics on the propagation of SIWs were investigated [27, 42]. Wavy surfaces having large dielectric constants and apexes with small radii of curvature produce electric field enhancement in the gas at the apexes. This electric field enhancement focuses gas phase IWs onto the surface, initiating SIWs. Charging of the surface may then launch both forward and reverse bulk IWs towards the electric enhancement of neighboring apexes. The same underlying mechanisms are expected, and observed, for acoustically shaped liquid surfaces. The E/N in the vicinity of the surface with a 15 kV applied voltage is shown in figure 8 for a 5 mM solution for flat ($n00$) and wavy surfaces ($n04$ to $n32$). These values are shown at 3 ns when the voltage is at its maximum value but prior to the plasma affecting potential distribution near the surface of the liquid. The high dielectric constant of the solution (ε_r 80) produces electric field enhancement at the apex of the waves and diminished E/N in the troughs of the wave. The diminished E/N results in part from the mild conductivity of the solution.

An added complication of shaped solutions compared to solid surfaces is the distribution of water vapor above the surface resulting from evaporation and gas flow. The densities of water vapor above the shaped surfaces are shown in figure 2 for surfaces $n00$ (flat) to $n32$ (wavelength 375 μm). The troughs of the waves contain stagnation zones, or regions that have weak vortices, that trap water vapor. The apexes of the waves are more exposed to the bulk flow which convects the water vapor away, and so have lower water vapor densities in their vicinities.

The electron density and electron-impact ionization sources are shown in figure 9 for the $n04$ structured surface for
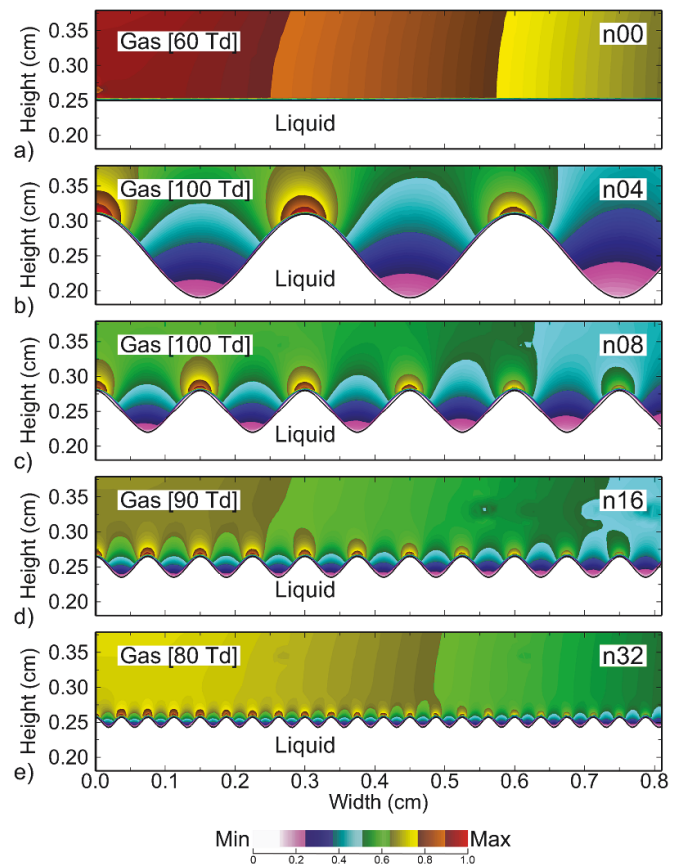

Figure 8. Electric field (E/N) across the solution surface at 3 ns for a 15 kV applied voltage with a 5 mM solution for structured surfaces. (a) $n00$, (b) $n04$, (c) $n08$, (d) $n16$, and (e) $n32$. The maximum value of E/N is noted in each frame.

a 15 kV pulse. Time sequences are shown for a 5 mM AgNO$_3$ solution, with a late-time comparison to a 25 mM solution. (The absolute value of the ionization sources is plotted. Regions labeled '/' and ' ' indicate net positive ionization and net electron loss.) The incident bulk IW that propagates from the electrode towards the surface is focused onto the on-axis apex of the surface due to the local electric field enhancement. The resulting propagation of the SIW is focused on (and near) the high electric field regions in the gas near the apexes of the waves. Similar to propagation of SIW over dielectric wavy surfaces, the surface of the mildly conductive solution charges at the site where the bulk IW strikes the surface. This charging then launches a bulk IW towards the electric field enhancement of the next apex. The IW strikes the next apex on its leading edge, largely bridging over the trough between apexes. The charging of the second wave produces a reverse IW back through the ionized channel, while also launching a bulk IW towards the next apex. The ionization source at 37 ns bridging the 3rd and 4th apexes in figure 9 results in large part from the reverse IW. VUV emission at the preceding peak illuminates and preionizes the gas near the leading surface of the following apex of the wave. Electrons released at the forward peak are then accelerated backwards through a positive space charge towards the preceding peak through the enhanced E/N. This process repeats, with the propagation of
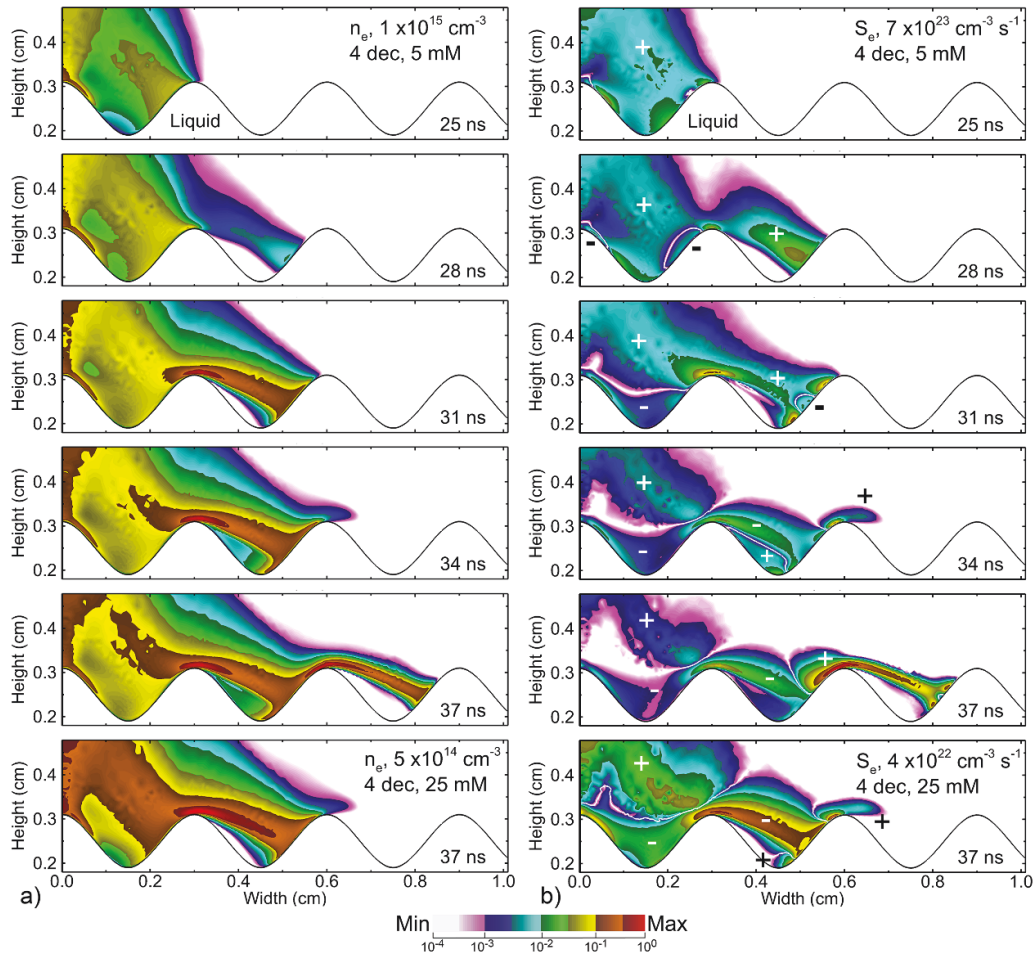
Figure 9. Macroscopic plasma properties for the *n*04 structured surface for a   15 kV pulse. Values are shown for 5 mM AgNO₃ solution for times of 25 ns–37 ns, and a 25 mM solution at 37 ns. (a) Electron density and (b) electron-impact ionization source, both with a 4-decade log scale. The absolute value of the electron-impact ionization source is plotted. The portions of the image labeled '+' and ' ' indicate regions of net electron source and loss.

the SIW being a series of hops originating at the apexes of the waves.

The deficiency in plasma density in the troughs of the waves arises in part due to the hopping of the IW from apex to apex and partly due to the large water vapor density in the troughs, leading to more diffuse volumetric VUV ionization at these locations. Although the IW waves are directed across the troughs, isotropic photoemission originating in the IWs does illuminate and photoionize both the water vapor and the liquid surface in the trough.

As the SIW passes from apex to apex, the ionization source is positive (net electron production). However, as the plasma channel is established and E/N decreases in the plasma channel, the electron source rapidly turns negative (net electron loss). The transition from electron source to electron loss is dominated by the reduction in E/N but is also exacerbated by the high water vapor density near the surface. This is particularly the case in the troughs where the water vapor density is the highest and into which the plasma does not significantly penetrate.

A similar sequence of SIW hopping occurs at higher solution molarity, shown by the results for the 25 mM solution in

figure 9. Similar to the flat surface, the SIW propagates across the higher conductivity 25 mM solution at a slower rate. The plasma is initially more focused on axis (as the plasma is for the flat surface). Requiring surface charging for propagation of the SIW, the more conductive solution is less able to support surface charging and sustaining the SIW.

The electron density and electron-impact ionization sources are shown in figure 10 for the *n*16 structured surface for a   15 kV pulse. Time sequences are shown for a 5 mM AgNO₃ solution, with a late-time comparison to a 25 mM solution. (The absolute value of the ionization sources is plotted. Regions labeled '/' and ' ' indicate net positive ionization and net electron loss.) The mode of propagation of the SIW across the structured surface is essentially the same as for the *n*04 surface—a hopping from apex to apex. However, with closer spacing of the apexes and more filling of the troughs with water vapor, there is less penetration of the plasma into the troughs. The SIW appears to propagate nearly uniformly across the surface. (Compare to the results for the flat, *n*00 surface in figure 4).

The mode of propagation of the SIW across the *n*16 surface is similar that of the *n*04 surface with increasing conductivity.
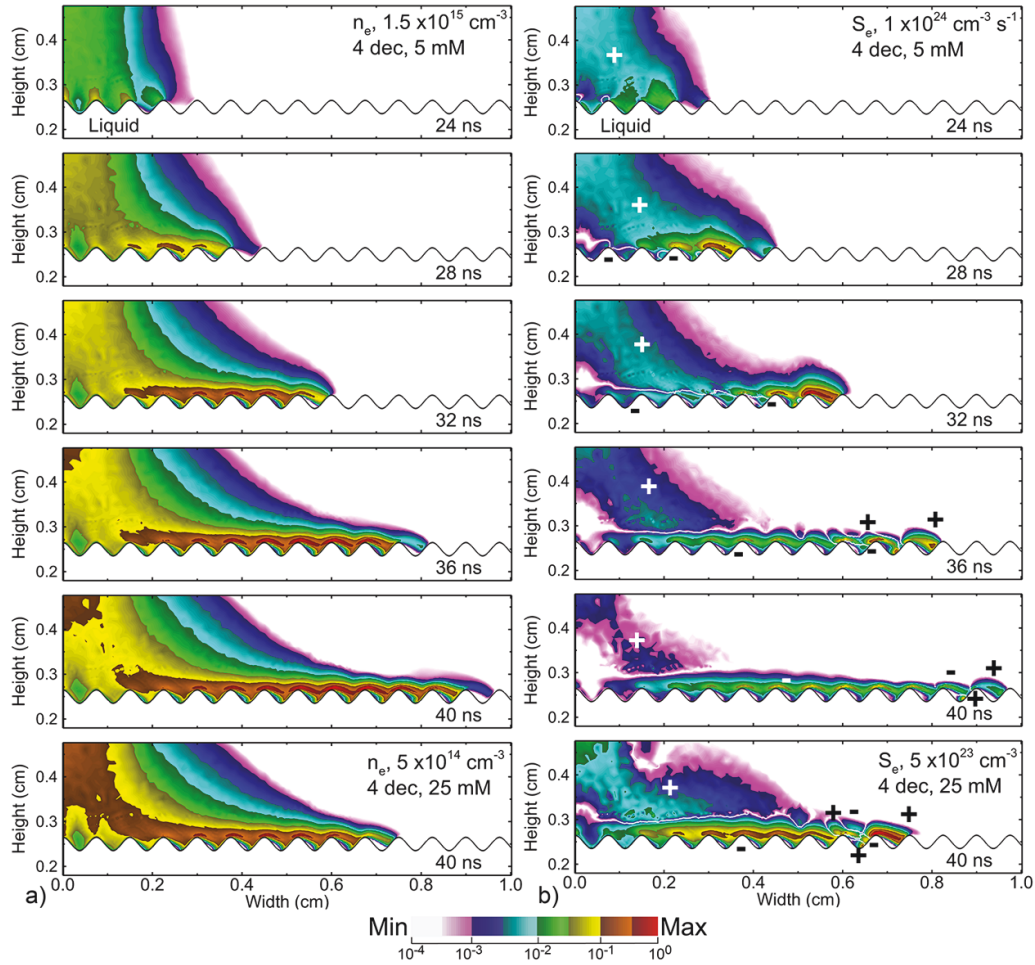
Figure 10. Macroscopic plasma properties for the *n*16 structured surface for a 15 kV pulse. Values are shown for 5 mM AgNO$_3$ solution for times of 24 ns–40 ns, and a 25 mM solution at 40 ns. (a) Electron density and (b) electron-impact ionization source, both with a 4-decade log scale. The absolute value of the electron-impact ionization source is plotted. The portions of the image labeled '+' and ' ' indicate regions of net electron source and loss.

The dominant effect is a slowing of the SIW laterally across the surface and a focusing of the SIW into the apex of the waves. These similarities aside, The SIW across the *n*16 surface is more sensitive to the conductivity of the solution compared to the *n*04 surfaces. As shown in figure 10 for the 25 mM solution, the propagation is more focused on the apexes of the waves, with there being hopping of the SIW from apex to apex. These trends result from the larger degree of electric field enhancement at the peaks of the waves with higher conductivity due to the smaller radius of curvature of the *n*16 surface. This electric field enhancement at the apexes is coincident with lower electric fields in the troughs with increasing conductivity due to the closer spacing of the peaks of the waves. These disparities, combined with the large water vapor density in the troughs, limits the propagation of the plasma across and into the troughs.

Electron fluence to the surface of the 5 mM and 25 mM AgNO$_3$ solutions integrated over 65 ns are shown in figure 11 for the flat (*n*00) and structured (*n*04, *n*08, *n*16, *n*32) surfaces. The discharge voltage is 15 kV. Fluences are plotted as a function of horizontal lateral position, allowing a direct comparison between the flat and structured surfaces. Note that the

fluences along the structured surfaces are calculated accounting for the increased path length.

Acoustic structuring of the liquid surface introduces periodic variations in the electron fluence to the surface, enhancing the fluence at the apexes of the waves and reducing the fluence in the troughs. These trends in fluence qualitatively agree with the distributions of electron density and ionization rates shown in figures 9 and 10. The enhancement in fluence at the peaks arises from the enhancement in *E*/*N* and local increases in ionization rate. The disparity between the maximum of electron fluence at the apex and the minimum in electron fluence in the trough increases with increasing wavenumber (and decreasing wavelength). For example, define β as the ratio of maximum electron fluence at the apex to the minimum fluence in the trough. Near a lateral position of 0.75 cm, β] 9, 18, 23, and 32 for the *n*04, *n*08, *n*16 and *n*32 surfaces. This modulation in electron fluence will produce spatially dependent densities of solvated electrons which in turn will initiate spatially dependent material synthesis in PDSE.

The modulation in electron fluence is greater for the higher conductivity 25 mM solution. The analogous values for the
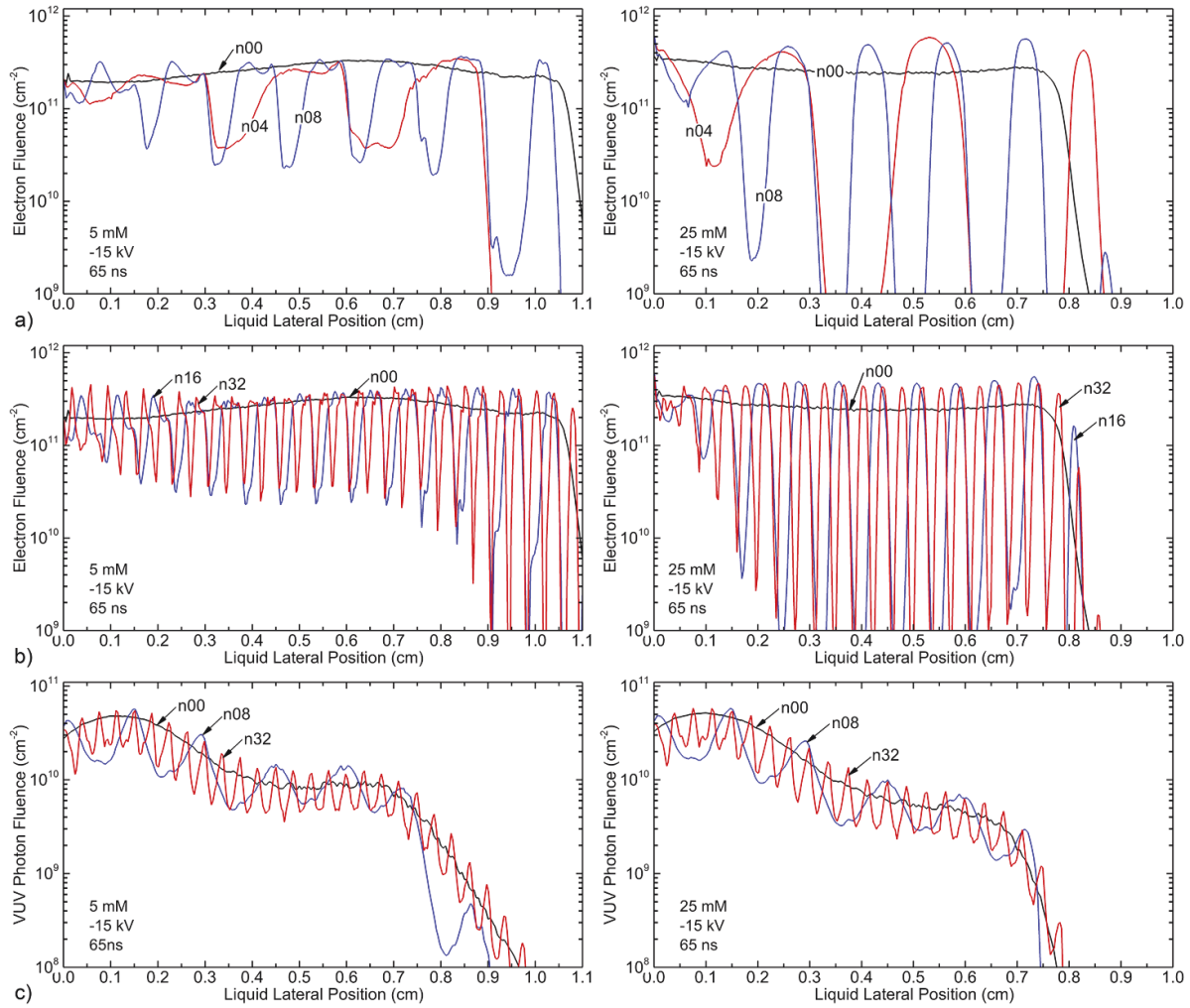
Figure 11. Fluences of electrons and photons over 65 ns for a   15 kV pulse onto 5 mM and 25 mM AgNO$_3$ solutions. Electron fluences for (a) n00, n04, and n08, and (b) n00, n16, and n32 structured surfaces. (c) VUV photon fluences for n00, n08, and n32 structured surfaces. The fluences are plotted as a function of horizontal lateral distance (and not distance along the surface). Note that the lateral extent in the images is 1.1 cm for the 5 mM solution and 1.0 cm for the 25 mM solution.

ratio of maximum to minimum electron fluence near 0.5 cm for the 25 mM solution are β] 5 ∼ 10^4, 10^5, 2300 and 580 for the n04, n08, n16, and n32 surfaces. These large values of β indicate that the troughs are essentially shadowed from the electron flux. The high conductivity waves are more conducive to apex-to-apex hoping and less conducive to SIW propagation into the troughs.

The VUV fluence is shown in figure 11(c) for the 5 mM and 25 mM solutions for the n00, n08 and n32 surfaces. The modulation in the VUV fluences apex-to-trough is only a factor of 2–3, a consequence of the long-mean-free path transport of the He$_2^*$ excimer radiation. These more uniform fluences imply that photolytically driven processes in solution will be less sensitive to the structuring of the surface.
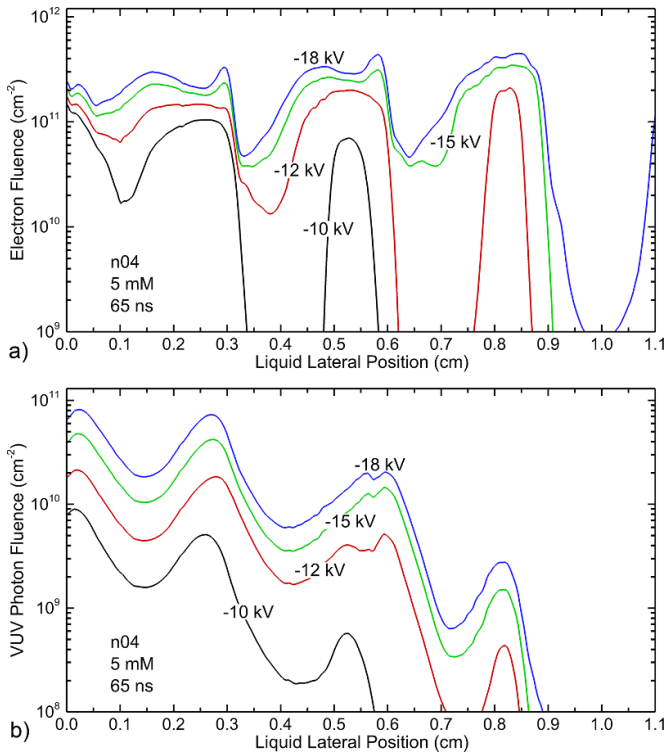
The total amount of potential activation of the solution by VUV and electron fluences is given by the spatial integral of the fluences shown in figure 11. If the PDSE process was strictly linear in the fluences of VUV and electrons (and ignoring depletion of the solute), then the total material produced would depend only on the spatial integral of these fluences.

The spatially integrated fluences (inventory) for VUV photons and electrons normalized by the value for the flat n00 surface are in table 2 for the 5 mM solution and n04 to n32 surfaces. The flat surface receives the largest inventory of both VUV photons and electrons. The n04 surface receives the smallest electron inventory (75% that of the flat surface) as the n04 surface has the largest relative modulation in fluences between peak and trough, and the largest local charging of the surface which would diminish electron fluences. The n32 surface has inventories closely resembling that of the flat surface. The electron inventories are more sensitive to the shape of the surface than VUV inventories. The VUV inventories vary by at most 9%. Electron fluences to the solution originate close to the surface and so are most sensitive to the shape and charging of the surface. VUV fluences originate several hundred microns or more from the surface, and so are less sensitive to local conditions.

Electron fluence and VUV fluence across the n04 liquid surface are shown in figure 12 for varying applied voltage for a 5 mM solution. As in the flat surface, increasing

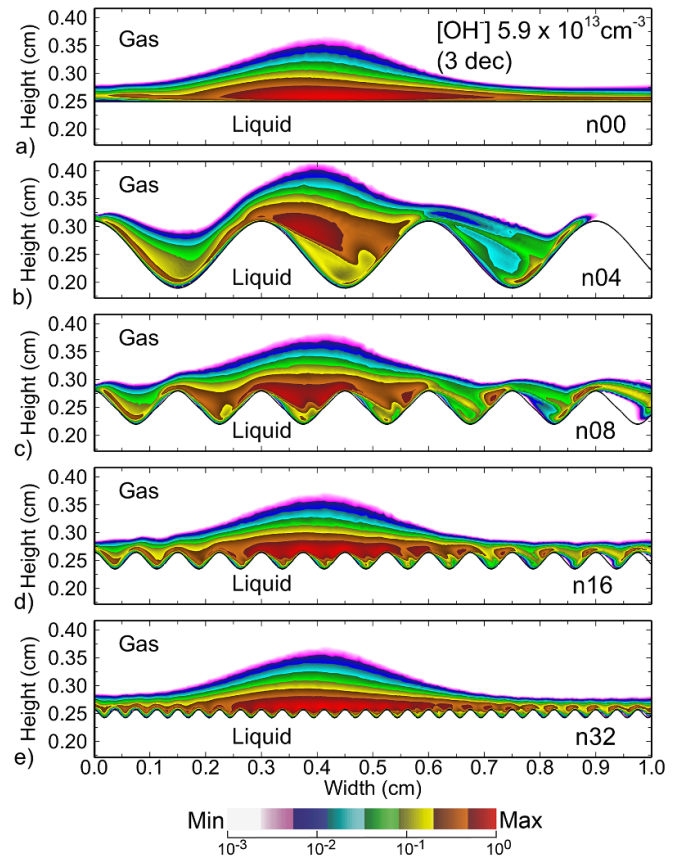**Table 2.** Spatially integrated fluences to the surface of the 5 mM solution relative to a flat surface ($n00$).

Surface	VUV photons	Electrons
$n04$	0.911	0.751
$n08$	0.943	0.853
$n16$	0.949	0.930
$n32$	0.968	0.983

Figure 12. Fluences of (a) electrons and (b) VUV photons across the $n04$ liquid surface at 65 ns for varying applied voltages and 5 mM AgNO$_3$ molarity.

the applied voltages enhances both the uniformity and the maximum extent of the SIW on the solution. For the lower voltages of 10 kV and 12 kV, the electron fluences are strongly focused near the apexes. For voltages of 15 kV and 18 kV, electrons can better propagate into the troughs, leading to a more uniform fluence. The VUV fluence increases significantly with voltage, but the overall shape is less affected than that of the electron fluences due to the non-local nature of the photon sources.

Structuring the liquid surface influences not only the reactivity delivered onto the surface but also the topology of reactive species produced in the gas phase. The distribution of the OH$^-$ ion above the liquid surface is shown in figure 13 for the flat and structured surfaces at the end of the pulse (65 ns). The profile resembles that of the electron density, albeit slightly more uniform. The distribution of O$^-$ is similar to OH$^-$, having a maximum density of $1.7 \sim 10^{13}$ cm^{-3} at 65 ns, approximately 3.5 times lower than OH$^-$.

The gas phase densities of OH and H$_2$O$_2$ after 2 μs are shown in figure 14 for the flat ($n00$) and structured ($n04$-$n32$)

Figure 13. Surface-adjacent OH$^-$ density at the end of the 15 kV pulse, $t = 65$ ns, for the flat (a) and structured (b)–(e) liquid surfaces, and a 5 mM AgNO$_3$ solution.

surfaces for the 5 mM solution. Even though the voltage pulse lasts only 65 ns, the profiles of OH and H$_2$O$_2$ after 2 μs closely mirror the profile of electron density left by the passage of the SIW. With the convective speeds above the surface no larger than 300–400 cm-s^{-1} and diffusions speeds even smaller, convective motion has yet to redistribute these species. The spatial distribution of other reactive oxygen species are similar to those for OH and H$_2$O$_2$. The local maxima in these densities (0.3–0.5 cm) reflect the maximum in plasma density in the SIW (see figure 4).

5. Selectivity of silver NP growth

In this section, we discuss how acoustically structuring the gas–liquid interface may provide control over silver NP production. The first step in NP growth is the reduction of silver cations, Ag$^+$, to neutral Ag in solution. The density distribution of silver neutral atoms (Ag$_{aq}$) at 50 ns is shown in figure 15(a) for all surfaces ($n00$-$n32$) and for a 25 mM AgNO$_3$ solution. In all cases, [Ag] peaks around 50 ns, reaching a value of approximately $6 \sim 10^{15}$ cm^{-3}. The profile of Ag neutral atoms on the flat liquid surface is nearly uniform along the first 0.2 cm, while on structured surfaces, the distribution of Ag is concentrated near the apexes indicating a spatial differentiation of reduction.
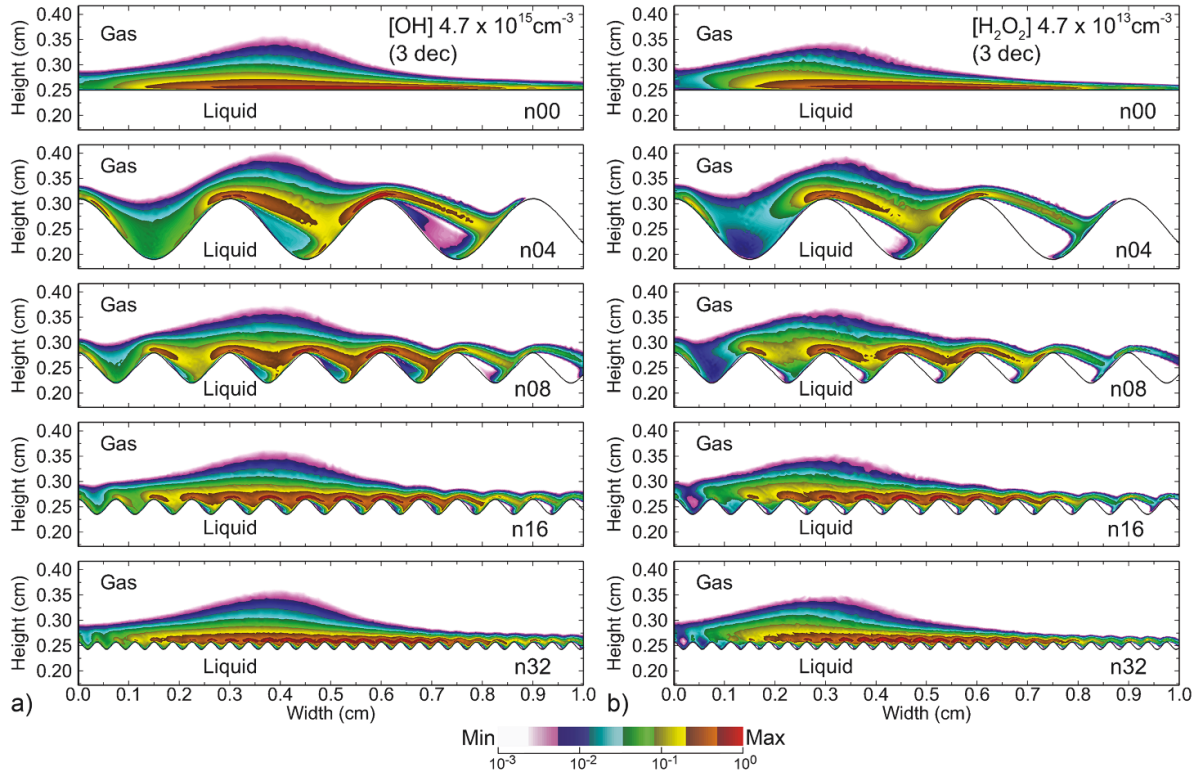
Figure 14. Surface-adjacent (a) OH and (b) H_2O_2 densities at $t = 2$ μs, after a single 15 kV pulse incident upon flat and structured liquid surfaces, for a 5 mM $AgNO_3$ solution.
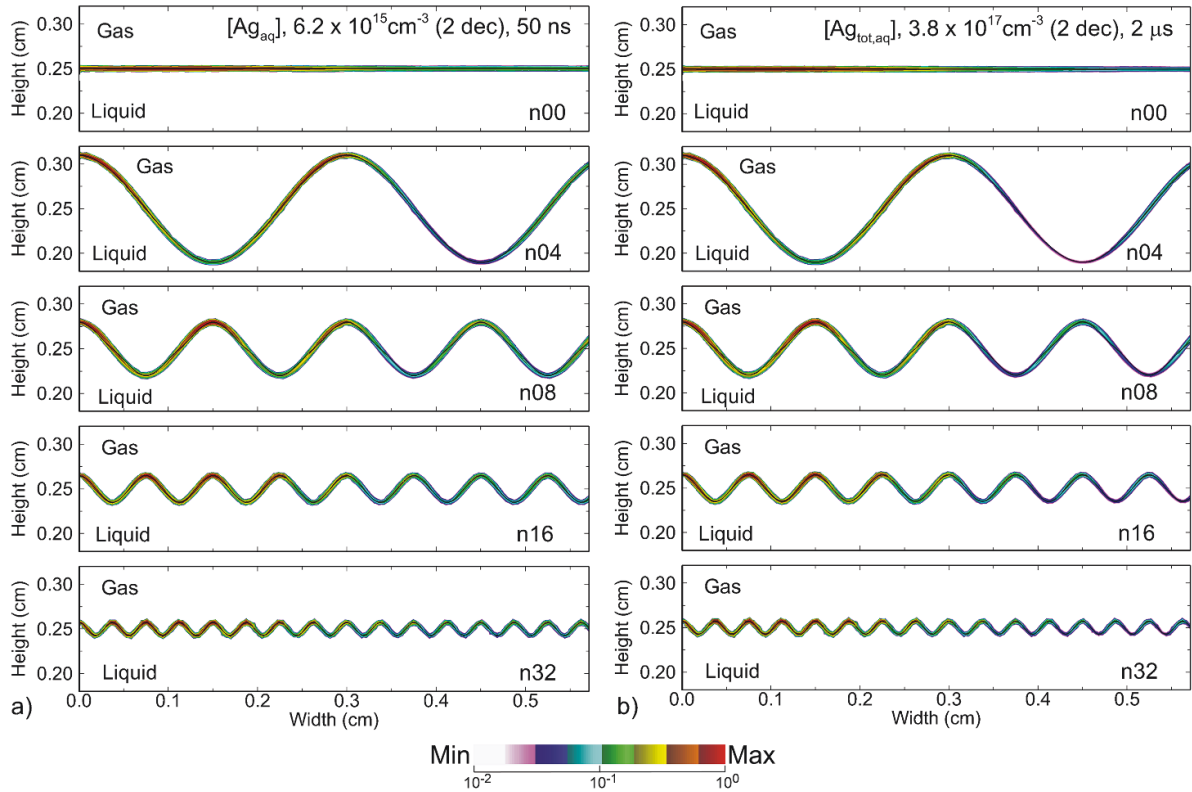

Figure 15. Densities of (a) silver neutral atoms, [Ag], and (b) total nucleated silver, $[Ag_{tot,aq}] = \sum_{n=2}^{4} \sum_{m} n \times [Ag_n^{m+}]$, for the various liquid surfaces and a 25 mM $AgNO_3$ solution. [Ag] is shown at 50 ns and $[Ag_{tot,aq}]$ is represented at 2 μs.

For example, let γ be the ratio between the Ag densities at the second centermost apex and the first centermost trough. At 50 ns, γ is 3.1, 3.3, 2.6, and 2.0 for the $n04$, $n08$, $n16$, and $n32$ surfaces, respectively. (For reference, on the flat ($n00$) surface, the ratio between [Ag] at $x \rceil$ 0.15 cm and at $x \rceil$ 0.075 cm is 0.96.) The behavior of γ is non-monotonic, increasing from $n04$ to $n08$ and then decreasing for higher wavenumbers. This trend is due to the competition of two effects: the higher the wavenumber, the smaller the radius of curvature of the apex, and the larger the electric field enhancement in the gas phase. However, as the wavenumber increases, the wavelength decreases, and the production of solvated electrons in the troughs by photoionization increases relative to direct electron fluxes.

The total densities of nucleated silver atoms, denoted as $[Ag_{tot,aq}] = \sum_{n=2}^{4}\sum_{m} n \times [Ag_n^{m+}]$, are shown in figure 15(b) for the liquid surfaces at 2 μs following a single 15 kV pulse. The distribution of $[Ag_{tot,aq}]$ closely mirrors the distribution of reduced silver atoms during the discharge, suggesting that acoustic structuring may aid in selectivity in NP production.

The temporal evolution of silver species is shown in figure 16 for the structured surfaces $n04$ through $n32$, comparing densities at the first centermost trough (dashed lines) and the second centermost apex (full lines). For reference, results are also shown for the flat $n00$ surface at the location of the trough of the $n04$ surface at 0.15 cm (denoted as [1]) and the peak of the $n04$ surface at 0.3 cm (denoted as [2]). In all cases, the Ag density (shown in figure 16(a)) begins increasing at approximately 20 ns, when the IW reaches the corresponding location and initiates the reduction of silver cations by producing solvated electrons in the solution. Around 40–50 ns, [Ag] reaches its peak and decreases thereafter. This depletion occurs due to the consumption of Ag neutral atoms in the formation of larger Ag molecules.

As shown in figure 16(b), the density of diatomic silver molecules in all charge states, $\sum_{m}[Ag_2^{m+}]$, begins increasing a few nanoseconds after the onset of formation of [Ag]. Then, the production of dimers sets the stage for the formation of trimers ($\sum_{m}[Ag_3^{m+}]$) and tetratomic ($\sum_{m}[Ag_4^{m+}]$) silver molecules, with the latter being shown in figure 16(c).

The flat surface does not have the spatial discrimination in fluxes provided by the troughs and peaks. The fluences of all electrons and VUV photons that produce reducing species generally continuously decrease with lateral location. The result is higher rates of nucleation near the axis.

The trends in nucleating precursors for Ag NPs following a single pulse using results from the 2D model indicate that NP size selectivity may be possible using structured liquid surfaces. However, NPs produced by PDSE usually result from treating the solution over tens of seconds (or longer). To investigate these timescales, the electron fluences produced by the 2D model were used as input to *GlobalKin*. The goal of these simulations is to isolate the effects of charged particles fluxes on NP production onto AgNO$_3$ solutions at different locations on the surface. To this end, in *GlobalKin*, only fluxes of electrons and H$_2$O$^+$, the ion dominating the positive ion flux, were
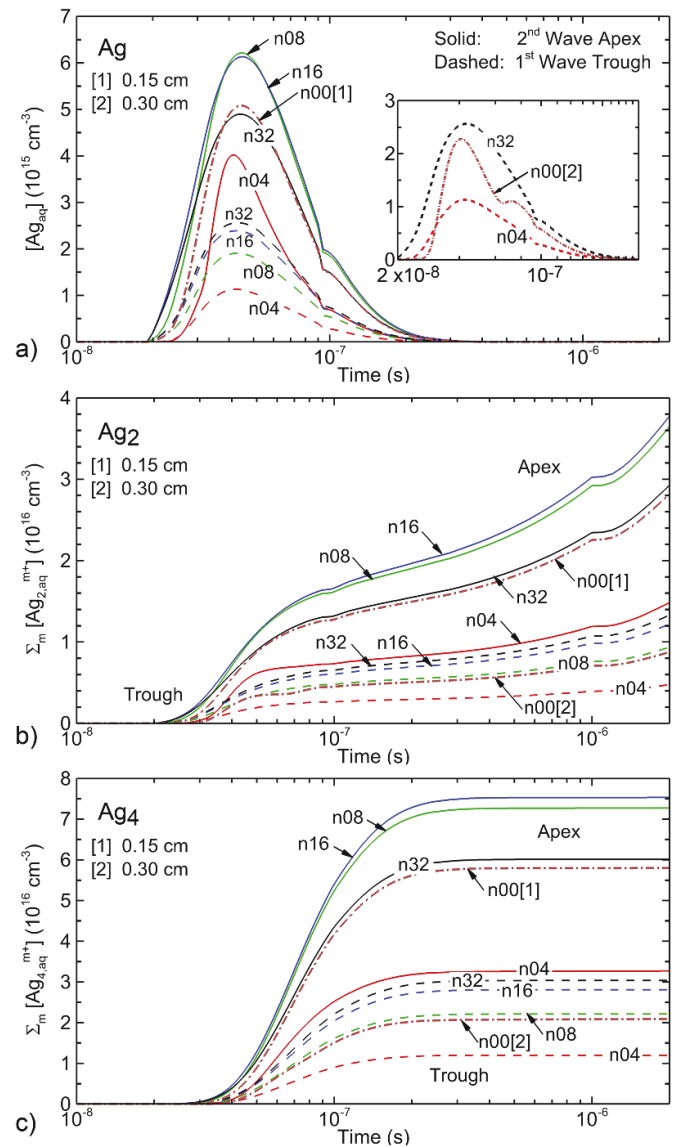

Figure 16. Time evolution of (a) [Ag], (b) $\sum_{m}[Ag_2^{m+}]$, and (c) $\sum_{m}[Ag_4^{m+}]$ at the first centermost trough (dashed lines) and the second centermost peak (full lines) for structured surfaces having $n04$-$n32$. For reference, results for the flat surface are shown for locations corresponding to [1] the trough of the $n04$ surface (0.15 cm) and [2] the peak of the $n04$ surface (0.3 cm). The solution contains 25 mM of AgNO$_3$.

directed onto the solution. The H$_2$O$^+$ flux was assumed to be equal to the electron flux produced by *nonPDPSIM*. Charged particle fluences at the apex and trough near a position of 0.6–0.7 cm were chosen for surfaces $n04$ to $n32$ and converted to time averaged fluxes for a PRF of 10 kHz. The resulting solution dynamics for production of Ag NPs were simulated for 100 s exposure for a 1 mm thick solution. The results from these simulations are in table 3 for 5 mM and 25 mM solutions.

For solvated electron dominated reduction, there are 3 regimes of particle nucleation and NP formation:

Table 3. Predicted Ag nanoparticle properties for $AgNO_3$ solution exposure for 100 s. (See the main text for the definition of the different regimes.)

				5 mM $AgNO_3$		
n	Position	e Flux ($cm^{-2}s^{-1}$)	Regime	NP	NP radius (nm)	NP density (cm^{-3})
$n04$	Apex	3.5×10^{15}	1	AgNP	21.8	7.5×10^{12}
$n04$	Trough	4.2×10^{14}	2	$AgNP^{3+}$	1.5	5.1×10^{12}
$n08$	Apex	3.6×10^{15}	1	AgNP	22.1	7.2×10^{12}
$n08$	Trough	2.1×10^{14}	2	$AgNP^{3+}$	0.9	1.2×10^{12}
$n16$	Apex	4.2×10^{15}	1	AgNP	22.3	7.0×10^{12}
$n16$	Trough	2.1×10^{14}	2	$AgNP^{3+}$	0.9	1.2×10^{12}
$n32$	Apex	4.2×10^{15}	1	AgNP	22.3	7.0×10^{12}
$n32$	Trough	8.3×10^{13}	2	$AgNP^{3+}$	0.6	2.3×10^{10}

				25 mM $AgNO_3$		
n	Position	e Flux ($cm^{-2}s^{-1}$)	Regime	NP/Cluster	NP radius (nm)	NP/Cluster density (cm^{-3})
$n04$	Apex	5.9×10^{15}	2	$AgNP^{3+}$	5.9	3.9×10^{14}
$n04$	Trough	3.0×10^{11}	3	Ag_2, Ag_4	—	3.1×10^{14}
$n08$	Apex	5.2×10^{15}	2	$AgNP^{3+}$	5.3	3.2×10^{14}
$n08$	Trough	6.8×10^{11}	3	Ag_2, Ag_4	—	6.9×10^{14}
$n16$	Apex	5.0×10^{15}	2	$AgNP^{3+}$	5.1	3.1×10^{14}
$n16$	Trough	4.7×10^{12}	3	Ag_2, Ag_4	—	4.8×10^{15}
$n32$	Apex	4.2×10^{15}	2	$AgNP^{3+}$	3.5	2.6×10^{14}
$n32$	Trough	3.1×10^{13}	3	Ag_2, Ag_4	—	3.2×10^{15}

(1) *Full reduction with neutral NPs*: The electron fluence over the treatment time can fully reduce the original inventory of Ag^+ cations. Ag_n^{m+} grow to a large enough size to produce NPs which, as a result of the full reduction, are largely neutral. NPs grow in size by agglomeration while reducing the density of NPs. NP growth is ultimately limited by Ostwald ripening. This regime occurs for high electron fluences relative to low molarity solutions.

(2) *Charged NPs:* The electron fluence is insufficient to fully reduce the inventory of Ag^+ cations but is large enough to produce NPs. Ag^+ has been converted to larger clusters. NPs increase in size by surface accretion of clusters and are charged due to the abundance of charged particle clusters. NPs also increase in density by reactions between Ag_n^{m+} and Ag_k^{j+} with $k / n > 9$. NP size is not limited by Ostwald ripening. This regime occurs for moderate electron fluences relative to high molarity solutions.

(3) *Sub-critical cluster growth*: Electron fluences are low while molarity is high. The large inventory of Ag^+ produces large densities of small charged clusters by Ag^+ reacting with Ag atoms produced by electron reduction. The rate of reaction of Ag_n^{m+} and Ag_k^{j+} with $k / n > 9$ is insufficient to produce NPs as small clusters are more likely to react with Ag^+ than with larger clusters.

For the 5 mM solution, the combination of electron fluxes to the apexes and exposure time enables full reduction of the Ag^+ inventory (Regime 1) for all surfaces. The NPs produced are largely neutral and limited in size by Ostwald ripening being approximately 22 nm in radius with densities of 7.0–$7.5 \sim 10^{12}$ cm^{-3}. The smaller fluxes incident onto the troughs

produce charged NPs (Regime 2). With a decrease in fluxes to the troughs with increasing wavenumber, the charged NPs radii decrease from 1.5 nm to 0.6 nm with decreasing densities of $5 \sim 10^{12}$ cm^{-3} to $2 \sim 10^{10}$ cm^{-3} for $n04$ to $n32$ surfaces.

For the 25 mM solution, the combination of electron fluxes to the apexes and exposure time does not fully reduce the Ag^+ inventory for any surface and produces charged NPs (Regime 2). With the higher molarity, reactions with solvated electrons are dominated by reduction of Ag^+ and small Ag_n^{m+} clusters, which results in smaller NPs, ranging from 5.9 nm to 3.5 nm for $n04$ to $n32$ surfaces. NPs are not produced by the smaller electron fluxes onto the troughs (Regime 3). This is particularly the case for the $n32$ surface in which the water vapor has a higher density in the troughs due to the troughs being largely stagnation zones. There is insufficient reduction of the Ag^+ inventory to produce the critical cluster sizes that generate NPs. The dominant clusters are Ag_2^{m+} and Ag_4^{m+}.

For every molarity, there is some combination of electron flux and exposure time (fluence) that will result in full reduction and neutral NP production. To some degree, the assignment of regimes is a sliding scale that moves towards Regime 1 with increasing electron fluence and towards Regime 3 with decreasing electron fluence. For example, for the 5 mM solution, fully reduced Regime 1 is reached at an exposure of 56 s at the apex of surface $n04$ and 43 s at the apex of surface $n32$.

The surface area of the solution in direct contact with the plasma is a function of the conductivity of the solution. Higher conductivity solutions with flat surfaces typically have smaller treated areas. Structuring the liquid surface offers a method whereby the area treated by the plasma may be altered independently of the solution molarity and conductivity. This

potentially enables larger areas of the liquid surface to be in contact with the plasma, producing more evenly distributed electron fluences when treating high conductivity solutions. This advantage is distinct from that of size selectivity.

6. Concluding remarks

Pulsed helium atmospheric plasma jets incident onto acoustically structured electrolytic liquids were computationally investigated using 2D and global models. The goal of the work was to demonstrate control of plasma produced fluxes (and fluences) to different locations on the surface of the solution based on the shape of the surface, here characterized by the wavenumber as might be produced by acoustic structuring. Control of these fluences then may enable control over material synthesis in PDSE systems. This control was achieved, with larger fluxes (fluences) delivered to the apexes of the waves and smaller fluxes delivered to the troughs of the waves. Through polarization of the $AgNO_3$ solutions and geometrical effects, electric fields in the gas phase were enhanced near the apexes of the waves and decreased in the troughs relative to flat surfaces, similar to non-planar solid dielectric surfaces. The modulation in E/N between the apex and trough varies in proportion to the liquid structure wavelength and amplitude, with the largest structures having the largest variation. Propagation of SIWs across the structured surfaces transitions to a hopping mode as the electric field enhancement at the apexes increases. At this juncture, the electron fluxes to apexes and troughs diverge. With increasing conductivity of the solution, electric field enhancement increases, as does the difference between fluxes delivered to apexes compared to troughs. These position dependent electron fluxes to the surface extend to VUV photon fluxes as well. However, the modulation in VUV fluxes is small compared to that for electrons. This smaller modulation results from electron fluxes being of largely local origin whereas VUV photon fluxes are of non-local origin.

The impact of the modulation of plasma produced fluxes to acoustically structured $AgNO_3$ solutions was evaluated by the predicted sizes and densities of silver clusters and NPs. Based on results of single-pulse simulations with the 2D model, higher order clustering of Ag_n^{m+} was produced with the larger electron fluences to apexes than troughs. These trends extended to global plasma chemistry simulations of NP growth over 100 s of exposure of structured $AgNO_3$ solutions having varying wavelengths and molarity. Three regimes were identified for NP growth: (1) full reduction producing larger neutral NPs, (2) partial reduction producing smaller charged NPs, and (3) lack of NP production. These growth regimes can be controlled by combinations of electron flux, exposure time, and solution molarity, the former of which can be controlled by the shape of the solution.

The ability to retain selectivity in synthesis of NPs by controlling fluences onto the solution in part depends on the transport of NPs in the solution. A solution that is well mixed during the length of plasma exposure required to synthesis the NPs will be challenged to maintain selectivity as the NPs will sample (and average) the spatially dependent fluences.

Ideally, solutions that are stagnant and resistant to forming convective cells would best retain the selectivity afforded by controlling fluences of plasma produced species onto the solution.

In actual plasma jet or DC discharge treatment during PDSE, the solution surface is rarely perfectly flat. Ripples and waves in the surface of the solution are often produced. The intentional outcomes of having acoustically structured surfaces—location dependent fluxes—are likely to naturally occur as a result of these ripples and waves in the surface of the solution. If these ripples and waves are random and chaotic (as is often the case), the location dependent fluxes are likely averaged over the duration of the plasma treatment. If the ripples and waves have some long-term stability or structure, then position dependent fluxes can be expected, leading to position dependent materials synthesis.

Data availability statement

The data that support the findings of this study are available upon reasonable request from the authors.

Acknowledgments

Conflict of interest

The authors have no conflicts of interest to report.

ORCID iDs

Scott J Doyle ⬤ https://orcid.org/0000-0002-8741-1018
Tiago C Dias ⬤ https://orcid.org/0000-0002-2179-1345
Mackenzie Meyer ⬤ https://orcid.org/0000-0002-2105-6690
Mark J Kushner ⬤ https://orcid.org/0000-0001-7437-8573

References

[1] Bruggeman P J *et al* 2021 Plasma-driven solution electrolysis *J. Appl. Phys.* **129** 1–19
[2] Adamovich I *et al* 2022 The 2022 plasma roadmap: low temperature plasma science and technology *J. Appl. Phys.* **55** 373001
[3] Bespalko S and Mizeraczyk J 2022 Energy balance of hydrogen production in the cathodic regime of plasma-driven solution electrolysis of Na_2CO_3 aqueous solution with argon carrier gas *Energies* **15** 9431
[4] Bespalko S and Mizeraczyk J 2022 Overview of the hydrogen production by plasma-driven solution electrolysis *Energies* **15** 7508
[5] Saksono N, Kartohardjono S and Yuniawati T 2016 High performance plasma electrolysis reactor for hydrogen *Int. J. Technol.* **8** 1421–9

[6] Yan Z C, Chen L and Wang H L 2006 Experimental study of plasma under-liquid electrolysis in hydrogen generation *Guocheng. Gongcheng. Xuebao/The Chin. J. Process. Eng.* **6** 396–401

[7] Mizuno T, Akimoto T, Azumi K, Ohmori T, Aoki Y and Takahashi A 2005 Hydrogen evolution by plasma electrolysis in aqueous solution *Jpn. J. Appl. Phys. 1* **44** 396–401

[8] Pattyn C, Maira N, Buddhadasa M, Vervloessem E, Iseni S, Roy N C, Remy A, Delplancke M P, DeGeyter N and Reniers F 2022 Disproportionation of nitrogen induced by DC plasma-driven electrolysis in a nitrogen atmosphere *Green Chem.* **24** 7100–12

[9] Toth J R, Hawtof R, Matthiesen D, Renner J N and Sankaran R M 2020 On the non-Faradaic hydrogen gas evolution from electrolytic reactions at the interface of a cathodic atmospheric-pressure microplasma and liquid water surface *J. Electrochem. Soc.* **167** 116504

[10] Delgado H E, Radomsky R C, Martin D C, Bartels D M, Rumbach P and Go D B 2019 Effect of competing oxidizing reactions and transport limitation on the Faradaic efficiency in plasma electrolysis *J. Electrochem. Soc.* **166** E181–6

[11] Lietz A M, Barnat E V, Foster J E and Kushner M J 2020 Ionization wave propagation in a He plasma jet in a controlled gas environment *J. Appl. Phys.* **128** 1–22

[12] Meesungnoen J, Jay-Gerin J P, Filali-Mouhim A and Mankhetkorn S 2002 Low-energy electron penetration range in liquid water *Radiat. Res.* **158** 657–60

[13] Akiyama N, Nakagawa Y, Uchida S and Tochikubo F 2021 Monte Carlo simulation of electrons injected from a low-temperature plasma into liquid water *J. Appl. Phys.* **129** 163304

[14] Rumbach P, Bartels D M, Sankaran R M and Go D B 2015 The solvation of electrons by an atmospheric-pressure plasma *Nat. Commun.* **6** 7248

[15] Gopalakrishnan R, Kawamura E, Lichtenberg A J, Lieberman M A and Graves D B 2016 Solvated electrons at the atmospheric pressure plasma-water anodic interface *J. Phys. D: Appl. Phys.* **49** 295205

[16] Khan I, Saeed K and Khan I 2017 Nanoparticles: properties, applications and toxicities *Arab. J. Chem.* **12** 908–31

[17] Xu C, Andaraarachchi H P, Xiong Z, Eslamisaray M A, Kushner M J and Kortshagen U R 2022 Size-tunable silver nanoparticle synthesis in glycerol driven by a low-pressure nonthermal plasma *J. Appl. Phys.* **56** 015201

[18] Hossain M M, Robinson N A, Mok Y S and Wu S 2023 Investigation of silver nanoparticle synthesis with various nonthermal plasma reactor configurations *Arab. J. Chem.* **16** 105174

[19] Lee S H and Jun B H 2019 Silver nanoparticles: synthesis and application for nanomedicine *Int. J. Mol. Sci.* **20** 865

[20] Iravani S, Korbekandi H, Mirmohammadi S V and Zolfaghari B 2014 Synthesis of silver nanoparticles: chemical, physical and biological methods *Res. Pharm. Sci.* **9** 385–406

[21] Jamkhande P G, Ghule N W, Bamer A H and Kalaskar M G 2019 Metal nanoparticles synthesis: an overview on methods of preparation, advantages and disadvantages, and applications *J. Drug Deliv. Sci. Technol.* **53** 101174

[22] Jin S-H, Kim S-M, Lee S-Y and Kim J-W 2014 Synthesis and characterization of silver nanoparticles using a solution plasma process *J. Nanosci. Nanotechnol.* **14** 8094–7

[23] Gamboa S M, Rojas E R, Martinez V V and Vega-Baudrit J 2019 Synthesis and characterization of silver nanoparticles and their application as an antibacterial agent *Int. J. Biosens. Bioelectron.* **5** 166–73

[24] Kortshagen U R, Sankaran R M, Pereira R N, Girshick S L, Wu J J and Aydil E S 2016 Nonthermal plasma synthesis of nanocrystals: fundamental principles, materials and applications *Chem. Rev.* **116** 11061–127

[25] Raisanen A L, Mueller C M, Chaudhuri S, Schatz G C and Kushner M J 2022 A reaction mechanism for plasma electrolysis of AgNO₃ forming silver nanoclusters and nanoparticles *J. Appl. Phys.* **132** 203302

[26] Weerasinghe J, Li W, Zhou R, Zhou R, Gissibl A, Sonar P, Speight R, Vasilev K and Ostrikov K K 2020 Bactericidal silver nanoparticles by atmospheric pressure solution plasma processing *Nanomaterials* **10** 1–10

[27] Konina K, Kruszelnicki J, Meyer M E and Kushner M J 2022 Surface ionization waves propagating over non-planar substrates: wavy surfaces, cut-pores and droplets *Plasma Sources Sci. Technol.* **31** 115001

[28] Norberg S 2015 Modelling atmospheric pressure plasma jets: plasma dynamics, interaction with dielectric surfaces, liquid layers, and cells *Doctoral Thesis* (available at: https://deepblue.lib.umich.edu/handle/2027.42/113342)

[29] Isowamwen O, Li R, Holsen T and Mededovic Thagard S 2023 Plasma-assisted degradation of a short-chain perfluoroalkyl substance (PFAS): perfluorobutane sulfonate (PFBS) *J. Hazard. Mater.* **456** 131691

[30] Bruggeman P J *et al* 2025 Advances in plasma-driven solution electrochemistry *J. Chem. Phys.* **162** 071001

[31] Jiang J and Bruggeman P J 2021 Absolute ion density measurementsin the afterglow of a radiofrequency atmospheric pressure plasma jet *J. Appl. Phys.* **54** 15LT01

[32] Van Gaens W and Bogaerts A 2014 Kinetic modelling for an atmospheric pressure argon plasma jet in humid air *J. Phys. D: Appl. Phys.* **47** 079502

[33] Norberg S A, Johnsen E and Kushner M J 2015 Formation of reactive oxygen and nitrogen species by repetitive negatively pulsed helium atmospheric pressure plasma jets propagating into humid air *Plasma Sources Sci. Technol.* **24** 035026

[34] Emmert F, Angermann H H, Dux R and Langhoff H 1988 Reaction kinetics of the He(2P) and the He₂* (a, v) states in high-density helium *J. Phys. D: Appl. Phys.* **21** 667–74

[35] Tian W and Kushner M J 2014 Atmospheric pressure dielectric barrier discharges interacting with liquid covered tissue *J. Phys. D: Appl. Phys.* **47** 165201

[36] Lietz A M and Kushner M J 2016 Air plasma treatment of liquid covered tissue: long timescale chemistry *J. Phys. D: Appl. Phys.* **49** 425204

[37] Meyer M, Nayak G, Bruggeman P J and Kushner M J 2023 HCOOₐq degradation in droplets by OHₐq in an atmospheric pressure glow discharge *J. Appl. Phys.* **56** 295205

[38] Itikawa Y and Mason N 2005 Cross sections for electron collisions with water molecules *J. Phys. Chem. Ref. Data* **34** 1–22

[39] Gentry S T, Kendra S F and Bezpalko M W 2011 Ostwald ripening in metallic nanoparticles: stochastic kinetics *J. Phys. Chem. C* **115** 12736–41

[40] Herrmann A, Margot J and Hamdan A 2024 Experimental investigation and 2D fluid simulation of a positive nanosecond discharge in air in contact with liquid at various dielectric permittivity and electrical conductivity values *Plasma Source Sci. Technol.* **33** 125009

[41] Laurita R, Barbieri D, Gherardi M, Columbo V and Lukes P 2015 Chemical analysis of reactive species and antimicrobial activity of water treated by nanosecond pulsed DBD air plasma *Clin. Plasma Med.* **3** 53

[42] Wang Q, Ning W, Dai D and Zhang Y 2020 How does the moderate wavy surface affect the discharge behavior in an atmospheric helium dielectric barrier discharge model? *Plasma Process. Polym.* **17** 1900182